

# ESO Imaging Survey

## I. Description of the survey, data reduction and reliability of the data

M. Nonino<sup>1,2</sup>, E. Bertin<sup>1,3,4</sup>, L. da Costa<sup>1</sup>, E. Deul<sup>1,3</sup>, T. Erben<sup>1,5</sup>, L. Olsen<sup>1,6</sup>, I. Prandoni<sup>1,7</sup>, M. Scodreggio<sup>1</sup>, A. Wicenec<sup>1</sup>, R. Wichmann<sup>1,8</sup>, C. Benoist<sup>1,9</sup>, W. Freudling<sup>10</sup>, M.D. Guarnieri<sup>1,11</sup>, I. Hook<sup>1</sup>, R. Hook<sup>10</sup>, R. Mendez<sup>1,12</sup>, S. Savaglio<sup>1</sup>, D. Silva<sup>1</sup>, and R. Slijkhuis<sup>1,3</sup>

<sup>1</sup> European Southern Observatory, Karl-Schwarzschild-Str. 2, D-85748 Garching b. München, Germany

<sup>2</sup> Osservatorio Astronomico di Trieste, Via G.B. Tiepolo 11, I-31144 Trieste, Italy

<sup>3</sup> Leiden Observatory, P.O. Box 9513, 2300 RA Leiden, The Netherlands

<sup>4</sup> Institut d'Astrophysique de Paris, 98bis Bd. Arago, F-75014 Paris, France

<sup>5</sup> Max-Planck Institut für Astrophysik, Postfach 1523 D-85748, Garching b. München, Germany

<sup>6</sup> Astronomisk Observatorium, Juliane Maries Vej 30, DK-2100 Copenhagen, Denmark

<sup>7</sup> Istituto di Radioastronomia del CNR, Via Gobetti 101, I-40129 Bologna, Italy

<sup>8</sup> Landensternwarte Heidelberg-Königstuhl, D-69117 Heidelberg, Germany

<sup>9</sup> DAEC, Observatoire de Paris-Meudon, 5 Pl. J. Janssen, F-92195 Meudon Cedex, France

<sup>10</sup> Space Telescope – European Coordinating Facility, Karl-Schwarzschild-Str. 2, D-85748 Garching b. München, Germany

<sup>11</sup> Osservatorio Astronomico di Pino Torinese, Strada Osservatorio 20, I-10025 Torino, Italy

<sup>12</sup> Cerro Tololo Inter-American Observatory, Casilla 603, La Serena, Chile

Received April 1; accepted December 21, 1998

**Abstract.** This paper presents the first data evaluation of the ESO Imaging Survey (EIS), a public survey being carried out by ESO and member states, in preparation for the VLT first-light. The survey goals, organization, strategy and observations are discussed and an overview is given of the survey pipeline developed to handle EIS data and produce object catalogs. A report is presented on moderately deep *I*-band observations obtained in the first of four patches surveyed, covering a region of 3.2 square degrees centered at  $\alpha \sim 22^{\text{h}}40^{\text{m}}$  and  $\delta = -40^\circ$ . The products available to the community, including pixel maps (with astrometric and photometric calibrations) and the corresponding object catalogs, are also described. In order to evaluate the quality of the data, preliminary estimates are presented for the star and galaxy number counts, and for the angular two-point correlation function obtained from the available data. The present work is meant as a preview of the final release of the EIS data that will become available later this year.

**Key words:** surveys — stars: statistics — galaxies: statistics

## 1. Introduction

With the advent of very large telescopes, such as the VLT, a largely unexplored domain of the universe becomes accessible to observations which may dramatically enhance our understanding of different physical phenomena, in particular the origin and evolution of galaxies and large scale structures. In the next few years a wide array of 8-m telescopes will become available world-wide. Among these, the European VLT project is particularly striking because of its four 8-m telescopes and an impressive array of complementary instrumentation. Viewed as a unit, the VLT provides great flexibility by combining complementarity for certain programs with multiplexing capabilities for others. First-light for the VLT is scheduled for May 1998, with regular science operation starting in April 1999.

In order to take full-advantage of the VLT from the start of its operation, ESO and its Observing Programmes Committee (OPC) decided to coordinate an imaging survey to provide candidate targets well-suited to the first set of VLT instruments. The ESO Imaging Survey (EIS) has been conceived as a collaborative effort between ESO and astronomers in its member states. Following the recommendation of the OPC, the survey has been overseen by a Working Group (WG). The EIS WG is composed of leading experts in different fields and has the responsibility of defining the survey science goals and strategy, and

monitor its progress. In order to carry out the survey a dedicated team was assembled, starting March 1997. To stimulate cooperation between ESO and the astronomical community of the member states, EIS has sponsored the participation of experts as well as students and post-docs from the community in the development of software, observations and data reduction.

As described by Renzini & da Costa (1997) (see also “<http://www.eso.org/eis>”), EIS consists of two parts: EIS-wide to search for rare objects (e.g., distant clusters and quasars) and EIS-deep to define samples of high-redshift galaxies. These science goals were chosen to match as well as possible the capabilities of the first VLT instruments, FORS, ISAAC and UVES. EIS is also an essential first step in the long-term effort, currently underway at ESO, to provide adequate imaging capabilities in support of VLT science (Renzini 1998). The investment made in EIS will be carried over to a Pilot Survey utilizing the ESO/MPIA 2.2 m telescope at La Silla, with its new wide-field camera. This Pilot Survey, which will follow the model of EIS, has been recommended by the EIS WG and is being submitted to the OPC.

The goal of this paper is to describe the characteristics of *I*-band observations carried out in the fall of 1997 over a region of 3.2 square degrees (EIS patch A, da Costa et al. 1998a) and of the corresponding data products, in the form of calibrated images and single frame catalogs. These products have been made publicly available through the ESO Science Archive, as a first step towards the full distribution of the EIS data. The purpose of the present release is also to provide potential users with a preview of the data, which may help them in the preparation of VLT proposals, and to encourage the community to provide constructive comments for the final release. It is important to emphasize that due to time limitations the results presented here should be viewed as preliminary and improvements are expected to be made before the final release of the EIS data later this year.

In Sect. 2, a brief description is presented of the criteria adopted in the field selection, the strategy of observations and the characteristics of the data in patch A already completed. It also describes the filters used, the definition of the EIS magnitude system and its relation to other systems, and the data used for the photometric calibration of the survey. In Sect. 3, a brief description of the data reduction pipeline is presented, followed in Sect. 4 by a description of the data products made publicly available in this preliminary data release. In Sect. 5, the algorithms used to detect and classify objects, and the information available in the catalogs being distributed are described. Preliminary results from a scientific evaluation of the data is presented in Sect. 6. In Sect. 7, future plans are presented, followed in Sect. 8 by a brief summary.

**Table 1.** Current sky coverage

Patch	$\alpha$	$\delta$	<i>B</i>	<i>V</i>	<i>I</i>
A	22:42:54	-39:57:32	-	1.2	3.2
B	00:49:25	-29:35:34	1.5	1.5	1.6
C	05:38:24	-23:51:00	-	-	6.0
D	09:51:36	-21:00:00	-	-	6.0
	-	-	1.5	2.7	16.8

## 2. The survey

### 2.1. Goals

EIS-wide is a relatively wide-angle survey of four pre-selected patches of sky, 6 square degrees each, spanning the right ascension range  $22^{\text{h}} < \alpha < 9^{\text{h}}$ . The main science goals of EIS-wide are the search for distant clusters and quasars. To achieve these goals the original proposal envisioned the observation of 24 square-degrees in *V* and *I*, 6 square degrees in *B* over one of the patches, and 2 square degrees in *U* in a region near the South Galactic Pole.

Because of the slow start of the survey due to the unusually bad weather caused by El Niño, which dramatically affected the observations in the period of July–November 1997, some of these goals had to be reassessed by the WG (da Costa et al. 1998a). It was decided to limit the observations to the *I*-band, except for patch B, the region close to the South Galactic Pole, where observations were conducted in *B*, *V* and *I* over 1.5 square degrees. The current status of the observations for EIS-wide is summarized in Table 1, where the J2000 centers of the actually surveyed patches and the area covered in the different bands are given.

EIS-deep is a multicolor survey in four optical and two infrared bands covering 75 arcmin<sup>2</sup> of the HST/Hubble Deep Field South (HDFS), including the WFPC2, STIS and NICMOS fields, and a region of 100 arcmin<sup>2</sup> in the direction of the southern hemisphere counterpart of the Lockman Hole, to produce samples with photometric redshifts to find *U*-dropout candidates and galaxies in the redshift range  $1 < z < 2$ . Observations for EIS-deep will start in August 1998 and therefore this part of the survey is not discussed in the present paper.

### 2.2. Field selection

The four EIS-wide patches were selected to have, in general, low optical extinction, low FIR ( $\lambda = 100 \mu$ ,  $A_V < 0.05$ ) emission and low HI column density ( $\sim 2 \cdot 10^{20} \text{ cm}^{-2}$ ). They were also examined to guarantee that they would not include very bright stars or nearby clusters of galaxies. Preference was also given to fields that would overlap with other interesting datasets, especially recently completed or ongoing wide-angle radio surveys (e.g., NVSS, Westerbork in the Southern

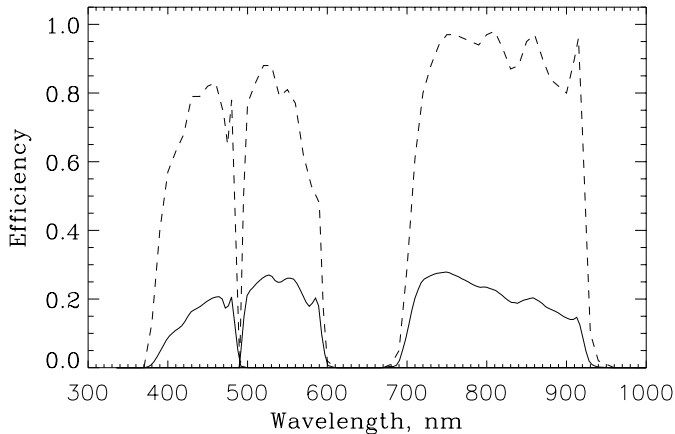


**Fig. 1.** Transmission curves for the EIS filters (dashed lines) and total system throughput including the contribution from the filters, telescope and camera optics, and the detector (solid lines)

Hemisphere, Australia Telescope ESO Slice Project). The fields were also chosen to cover a range of galactic latitudes of possible interest for galactic studies. A map showing the position of the EIS patches and overlapping surveys can be found in the EIS web-pages (“<http://www.eso.org/eis>”).

### 2.3. EIS filters

Since the primary consideration in the selection of the filters was the desire for depth, the observations were conducted using wide-passband filters. EIS uses a special set of  $BVI_c$  filters (ESO WB430 # 795, WB539 # 796, WB829 # 797), which were designed to have higher transmission than the  $BVI_c$  passbands. The transmission curves for the filters and the full response of the NTT-EMMI red system with the EIS filters are shown in Fig. 1, and can be retrieved in electronic form from the World Wide Web at “[http://www.eso.org/eis/eis\\_filters.html](http://www.eso.org/eis/eis_filters.html)”.

While the effective wavelengths of these filters are close to those of the Johnson-Cousins  $BVI_c$  filters, their passbands are broader and have sharper cutoffs. The measured passbands of these filters have been used to derive synthetic photometry using the Gunn & Stryker (1983) catalog of spectrophotometric scans of main-sequence and giant stars. For WB430 # 795 ( $B$  band) the throughput was determined to be 0.42 mag higher than Johnson  $B$  (at  $B - V = 0$ ), and for WB829 # 797 0.44 mag higher than Cousins  $I_c$  (at  $V - I_c = 0$ ). However, the WB539 # 796 filter turned out to have a throughput slightly lower (0.18 mag) than Johnson  $V$ .

### 2.4. Survey strategy

The observations for EIS-wide started in July 1997 and are being conducted using the EMMI camera (D’Odorico

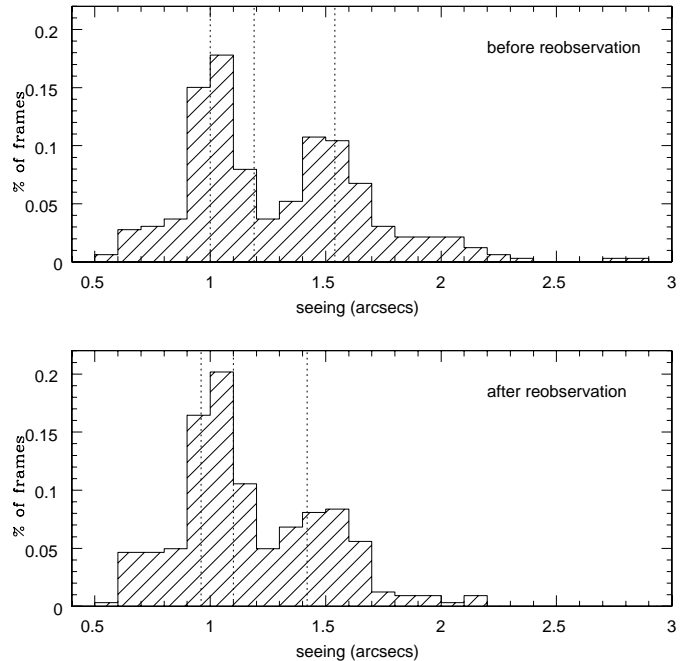


**Fig. 2.** Seeing distribution for patch A obtained from all observed frames (top panel) and only from the frames actually accepted for the survey (bottom panel). Vertical lines refer to 25, 50 and 75 percentiles of the distributions

1990) mounted on the 3.5-m New Technology Telescope (NTT) at La Silla. The EMMI red channel is equipped with a Tektronix  $2046 \times 2046$  chip with a pixel size of 0.266 arcsec and an effective field-of-view of about  $9' \times 8.5'$ , because of the strong vignetting at the top and bottom parts of the CCD. In order to cover a large area of the sky the observations are being conducted using a sequence of 150 s exposures shifted by half the size of an EMMI-field both in right ascension and in declination. This leads to an image mosaic whereby each position in the sky is observed twice for a total integration time of 300 s, except at the edges of the patch. The easiest way of visualizing the geometry of the EIS mosaic is to picture two independent sets of tiles (referred to as  $P_{i,j}$ , where  $i$  refers to the row along right ascension and  $j$  to columns in declination) forming a contiguous grid (normally referred to as odd and even depending on the value of  $j$ , and  $P$  is the patch name A-D) superposed and shifted in right ascension and declination by half the width of an EMMI frame. To ensure continuous coverage, adjacent odd/even frames have a small overlap at the edges ( $\sim 20$  arcsec). Therefore, a small fraction of the surveyed area may be covered by more than two frames. Such a mosaic ensures good astrometry, relative photometry and the satisfactory removal of cosmic ray hits and other artifacts.

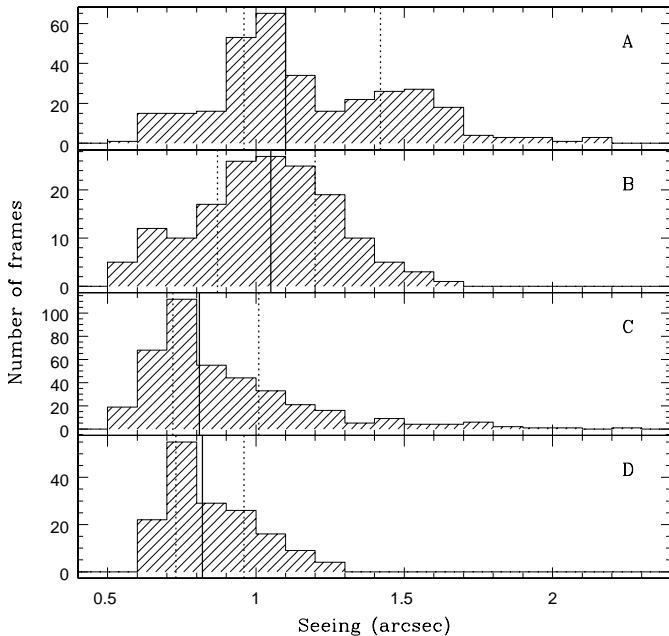


**Fig. 3.** Seeing distribution for all the EIS patches. The plot includes all the data taken in 1997. Note the great improvement of the seeing distribution, especially for patches C and D

### 2.5. Observations

Because of bad weather conditions, for patch A it was only possible to cover 3.2 square degrees in the  $I$ -band and 1.2 square degrees in the  $V$ -band. These observations were obtained in six different runs in the fall of 1997. The observations were carried out in standard visitor mode and data were taken in less than ideal conditions. A total of 400 science frames were obtained in  $I$ -band for patch A with the seeing varying from about 0.6 arcsec to over 2 arcsec. Regions observed under poor conditions were re-observed to maintain some degree of uniformity in the depth of the survey. In Fig. 2 the seeing distribution of all frames obtained in patch A (top panel) and of the frames actually accepted for the survey (bottom panel) are compared. This gives an idea of the area which required re-observations ( $\lesssim 1$  square degree) and the impact that these had on the early progress of the survey. The median seeing for all frames is about 1.2 arcsec, while for the accepted frames it is about 1.1 arcsec. More importantly, the fraction of frames with seeing greater than 1.5 arcsec was greatly reduced. Note that the observing conditions have varied considerably within a run and from run to run during the period of observations of patch A, with only a small number of photometric nights. Therefore, depending on the application it may be necessary to further filter the object catalogs according to the characteristics of the data (Sect. 6.3). While this is trivial when dealing with single frames, proper pruning of the data requires more sophisticated tools when considering catalogs produced from the coadded image.

It is worth emphasizing that the data for patch A are by far the worst. This can be seen in Fig. 3, where the seeing distribution for patch A is compared with that of the other patches.

During EIS nights photometric and spectrophotometric standards are regularly observed (Landolt 1992a; Baldwin & Stone 1984; Landolt 1992b). Whenever possible, photometric solutions are derived to evaluate the quality of the night and to determine absolute zero-points for the tiles observed during photometric nights.

The photometric quality of the nights is also being assessed from the observations conducted by the Geneva Observatory at the 0.7 m Swiss telescope, which regularly monitors the extinction coefficients at La Silla. The information from the Swiss telescope is stored in a calibration database to provide the necessary reference with the survey nights. Whenever this information is available, images taken during photometric nights are flagged, and this information is used in the absolute photometric calibration of the patch (Sect. 3.9).

### 2.6. EIS magnitude system

The zero-points of the EIS magnitude system have been defined to give the same  $B$ ,  $V$ ,  $I$  magnitudes as in the Landolt system for stellar objects with  $(B - V) = (V - I_c) = 0$ . In other words, EIS magnitudes are by definition equal to the magnitudes in the Johnson-Cousins system for zero-color stars.

In Fig. 4 we show the observed transformation between the EIS system and Johnson-Cousins for the  $I$ -band, as a function of color. The data points are based on all the reduced observations of standard stars currently available (run 1-7). From a linear fit to the data points the color term between the EIS and Cousins system is found to be small ( $0.014 \pm 0.004$ ). Note, however, that because of the limited amount of photometric nights up to run 7, color terms have not yet been taken into account in the photometric solutions, and the current  $I$ -band zero-point of the EIS system may be subject to small changes ( $\sim 0.01$  mag) at a later date, when more data becomes available in the final release.

### 2.7. External data

In order to provide additional constraints on the absolute calibration of the survey, data were obtained under photometric conditions from other telescopes at La Silla. Observations were conducted at the 2.2 m telescope (4 half-nights, out of which one half-night under photometric conditions) and one night at the 0.9 m Dutch telescope.

The observations with the 2.2 m telescope were carried out using EFOSC2 with a  $2048 \times 2048$  CCD chip,

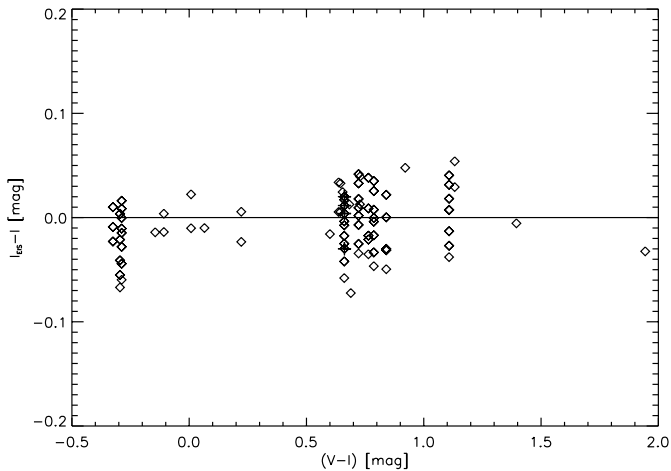


**Fig. 4.** Relation between the EIS and Johnson-Cousins system as a function of Johnson-Cousins color. Shown are all the standard stars observed under photometric conditions in the period July 97-January 98

with a pixel size of 0.27 arcsec and a seeing of about 1.5 arcsec. The filters used in these observations were ESO # 583, ESO # 584, ESO # 618. EFOSC2 has a field of view  $8.3' \times 7.7'$ . During observations of the only photometric night, standard stars and frames over the original area of patch A were obtained in *B*, *V* and *I*. Unfortunately, only two *I*-band images overlap with the surveyed area, as shown in Fig. 5. The limiting magnitude of the frames is  $I \sim 20$ . Over 100 objects per frame were found in common with the overlapping survey fields.

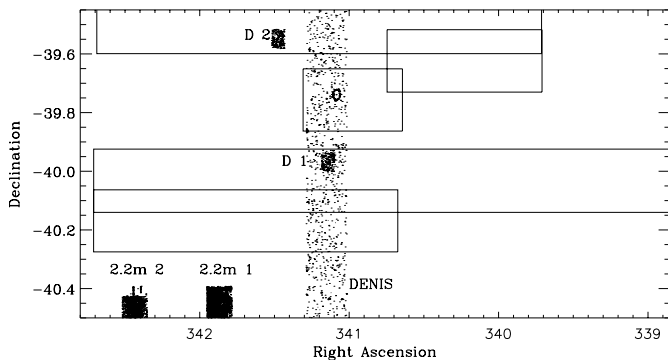


**Fig. 5.** Distribution of frames obtained at the 2.2 m and the 0.9 m Dutch (D) telescopes at La Silla within the covered region of patch A. Also shown is a part of a DENIS strip that crosses the field. The open rectangles represent regions containing EIS tiles observed under photometric conditions

The observations with the 0.9 m Dutch telescope were done in one photometric night using TK512CB (a  $512 \times 512$  CCD chip, with a pixel size of 0.47 arcsec) at a seeing of about 1.5 arcsec. The field of view approximates one quarter of an EIS survey tile, i.e.  $3.1' \times 4.0'$ . The filters used were ESO # 419, ESO # 420, and ESO # 465.

The limiting magnitude of the science frames is  $I \sim 22$ . Approximately 200 objects per frame were found in common with the overlapping EIS survey tiles for the range  $14 < I < 22$  to define the zero-point.

Images from both telescopes were processed in a standard way using IRAF. One major problem was the severe fringing observed in the *I*-band frames from the 2.2 m. The fringing was removed by creating a combination of the 300 s science exposures and using IRAF's `mkfringcor` task, but preliminary results show that this correction may have affected the measurement of faint objects.

In addition to these scattered fields, a reduced strip of *I*-band data from the DENIS survey (Epchtein et al. 1996) is also available. Unfortunately, close inspection of the data showed that the strip was observed in non-photometric conditions.

Figure 5 shows the overlap of the external data with the surveyed region. Also shown are the regions covered by EIS tiles observed in photometric conditions.

### 3. Data reduction

#### 3.1. Overview of the EIS pipeline

An integral part of the EIS project has been the development of an automated pipeline to handle and reduce the large volume of data generated by EIS. The pipeline consists of different modules built from pre-existing software consisting of: 1) standard IRAF tools for the initial processing of each input image and preparation of superflats; 2) the Leiden Data Analysis Center (LDAC) software, developed for the DENIS (Epchtein et al. 1996) project to perform photometric and astrometric calibrations; 3) the SExtractor object detection and classification code (Bertin & Arnouts 1996); 4) the “drizzle” image coaddition software (Fruchter & Hook 1997; Hook & Fruchter 1997), originally developed for HST, to create coadded output images from the many, overlapping input frames.

A major aim of the EIS software is to handle the generic problem posed by the building up of a mosaic of overlapping images, with varying characteristics, and the extraction of information from the resulting inhomogeneous coadded frames. This has required significant changes in the preexisting software. To illustrate the power of the tool being developed a brief description of the basic idea behind the pipeline is necessary. For each input frame a weight map, which contains information about the noise properties of the frame, and a flag map, which contains information about the pixels that should be masked such as bad pixels and likely cosmic ray hits, are produced. After background subtraction and astrometric and relative photometric calibration, each input frame is mapped to a flux-preserving conic equal-area projection grid, chosen to minimize distortion in area and shape of objects

across the relatively large EIS patch. The flux of each pixel of the input frame is redistributed in the superimage and coadded according to weight and flags of the input frames contributing to the same region of the coadded image. Therefore, the coaddition is carried out on a pixel-by-pixel basis. It is clear that in the process the information about the individual input frames is lost and in order to trace them back an associated context (domain) map is created, providing the required cross-reference between the object and the input frames that have contributed to its final flux. Another important output is the combined weight map which provides the required information to the object detection algorithm to adapt the threshold of source extraction to the noise properties of the context being analyzed. SExtractor has been extensively modified for EIS and its new version incorporates this adaptive thresholding (new SExtractor documentation and software are available at “<http://www.eso.org/eis>”). For a survey such as EIS, being carried out in visitor mode with varying seeing conditions, this cross-reference is essential as it may not be possible to easily characterize the PSF in the final coadded image, a problem which in turn affects the galaxy/star classification algorithm.

In the present paper the main focus is on the processing and the object catalogs extracted from the individual frames that make up the mosaic and which provide a full contiguous coverage of patch A with well defined characteristics.

### 3.2. Retrieving raw data

EIS utilizes the observational and the technical capabilities of the refurbished NTT and of the ESO Data Flow System (DFS), from the preparation of the observations to the final archiving of the data. DFS represents an important tool for large observational programs. The ESO Archive is interfaced with the EIS pipeline at both ends: it supplies the observed raw data and collects the output catalogs and reduced images.

In the course of delivering the data to EIS, the raw data is also archived in the ESO NTT Archive. The headers of the data delivered to EIS had to be adjusted in a variety of ways to meet the requirements of the EIS pipeline. Since standard ESO FITS-headers contain a wealth of instrumental and observational parameters in special ESO keywords, translation of some of these keywords to user defined keywords is a standard tool the Archive offers. Header translation was executed automatically right after the transfer of every single file. Moreover the files were renamed and sorted into subdirectories to reflect the nature of the frames (calibration, science and test frames). Filenames have been constructed which ensured both uniqueness and a meaningful description of the observed EIS tile, filter and exposure. Most of the important parameters of all transferred files are ingested into several

database tables, briefly described below, which serve as a pool of information used during the execution of the pipeline. The database also provides all the information necessary to characterize the observations.

### 3.3. Frame processing

The EMMI frames have been read in a two-port readout mode. The assumed gain difference between the two amplifiers is about 10% ( $2.4 \text{ e}^-/\text{ADU}$ ,  $2.16 \text{ e}^-/\text{ADU}$ ), with a readout noise of  $5.49 \text{ e}^-$  and  $5.81 \text{ e}^-$ , as reported by the NTT team. Slight variations of this value have been detected from run to run. Currently, standard IRAF tools are used to remove the instrumental signature from each frame. To handle the dual-port readout, pre-scan corrections are applied for each half-frame using the *xccdred* package of IRAF by subtracting a fitted pre-scan value for each row.

A master bias for each run is created by median combining all bias frames, typically  $\gtrsim 50$  per run, using the  $3\text{-}\sigma$  clipping option. The effective area used in this calculation is from Cols. 800 to 2000 (along the  $x$ -axis) and rows from 100 to 1900 (along the  $y$ -axis), which avoids a bad column visible at the upper part of the chip and vignetted regions on top and bottom of the image. The same procedure is adopted for the dome flats. About 10 dome flats for each filter were used with about 15 000 ADUs. Skyflats were obtained at the beginning and end of each night using an appropriate calibration template to account for the variation of sky brightness in each band so that about five skyflats per night were obtained with 40 000 ADUs. These bright sky exposures were monitored automatically to reject those frames which could have been saturated or that had low S/N. The skyflats were combined using a median filter on a run basis and then median-filtered within a  $15 \times 15$  pixel box.

For each science frame a pre-scan correction is made and the frames are trimmed making the usable area of the chip from row 21 to 2066 ( $x$ -axis) and from Col. 1 to 2007 ( $y$ -axis). Note that this procedure does not completely remove the vignetted region of the frame or a coating defect visible on the chip. As will be seen later a suitable mask is defined to handle these regions. After trimming, the combined bias is subtracted and the frames are flat-fielded using the dome flats, and an illumination correction is applied using the combined skyflats.

After each survey frame has been corrected for these instrumental effects, a quick inspection is carried out by eye. A single EIS keyword is set in the header to flag those frames which contain satellite tracks, bright star(s), background gradients due to nearby bright objects, or those useless for scientific purposes (e.g., those affected by motions of the EMMI rotator or by glitches in the tracking leading to double or even triple images). Flagged frames are then rejected during the creation of the supersky flat,

which is obtained from the combination of all suitable science frames using a median filter and  $3\sigma$  clipping. The superflat is created on a run basis and is smoothed using a running box  $15 \times 15$  pixels in size.

During visual inspection masks are also created and saved for use by the pipeline (Sect. 3.7) to mark regions affected by bright stars just outside the frame, some satellite tracks or cosmic rays in the form of long streaks in the frame. This can be done by taking advantage of features recently implemented in the SkyCat display tool (Brighton 1998, see also “<http://www.eso.org/eis>”).

Finally, the superflat is applied to both the survey and standard star frames taken during the night. The low-resolution background images (minibacks, see Sect. 5.1.1) generated by SExtractor, prior to the source extraction (minibacks), have been used to estimate the homogeneity of the resulting science images. In general, the flatness of the images is  $\lesssim 0.2\%$ , except for two runs for which larger values (up to  $\sim 1.4\%$ ) are found. A major contribution to the background residual is probably due to variations in the relative gain of the two readout ports, which will be investigated further.

Note that the flat-fielding of EIS images is done in *surface brightness*, not in *flux*. Variations of the pixel scale over the field may cause a drift of the magnitudes, especially at the edges of the frames. However, distortions lead to a variation of pixel-scale which has been estimated from the astrometric solution (Sect. 3.8) to be  $\lesssim 0.5\%$ . This translates to a photometric drift  $\lesssim 0.01$  mag, over the field, which has not been corrected for in the present release.

### 3.4. Processing standard stars

Frames for standard stars are also processed automatically through a parallel branch of the pipeline fine-tuned to process standard star fields. Reference catalogs for all the Landolt fields are available and are used to pair objects and identify the standard stars. Aperture photometry, using Landolt apertures, is carried out and extinction coefficients and zero-points are computed and stored in the calibration database together with other observational parameters. Plots are also produced to ease the task of identifying photometric nights. The automatic process has been checked against reductions carried out manually with IRAF tasks, yielding consistent results.

### 3.5. Survey monitoring and quality control

An integral part of the survey pipeline is the automatic production of reports for the monitoring of the data and the data reduction, and for diagnosing the different tasks of the EIS pipeline. These reports produce several plots that are interfaced with the WEB, for easy access by the

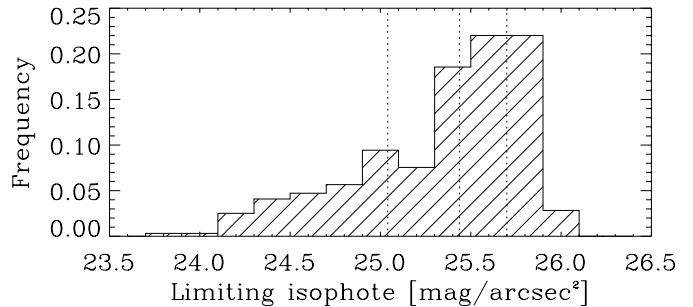


**Fig. 6.** Limiting isophote distribution for the patch A frames actually accepted for the survey. Vertical lines refer to 25, 50 and 75 percentiles of the distributions

EIS team. They can also be retrieved at a later time from information available in the EIS database (Sect. 3.6).

From the raw data retrieved from the archive a set of plots is produced which provides information on: 1) the time-sequence of observations (which has helped optimize the use of the DFS, and monitor the efficiency of the observations); 2) the performance of the pointing model; 3) the continuity of the coverage of the patch (by monitoring the overlap between tiles); and 4) the observed tiles and repeated observations.

After processing the data another set of plots is produced which show the seeing as measured on the images, the number counts at a fixed limiting magnitude, the limiting magnitude, defined as the  $5\sigma$  detection threshold for a point source, and the  $1\sigma$  limiting isophote ( $\text{mag}/\text{arcsec}^2$ ). As an illustration Fig. 6 shows the distribution of the limiting isophote for the accepted tiles of patch A, and Figs. 7 and 8 show the two-dimensional distribution of the seeing and limiting isophote. These plots are useful to guide the selection of regions for different types of analysis. Diagnostic plots are also produced after the astrometric calibration of the frames, and before and after the calculation of the relative and the absolute photometric calibration.

Based on this information the observing plans for subsequent runs are reviewed. In the case of patch A, originally observed under poor conditions, an attempt was made to improve the quality of the data as discussed earlier (see Fig. 2).

The image quality of the survey frames has also been monitored by computing the size and anisotropy of the PSF for suitably chosen stars covering the survey frames. While this in principle could be done directly from the catalogs produced by the pipeline, the second order moments of the brightness distribution produced by the current version of SExtractor are sensitive to noise which affect the measurement of object shapes. Therefore, to monitor the shape of the PSF the software developed by Kaiser et al. (1995) (hereafter KSB) has been used. It computes the shape of objects by using appropriate weights in the calculation of the second order moments. Comparison

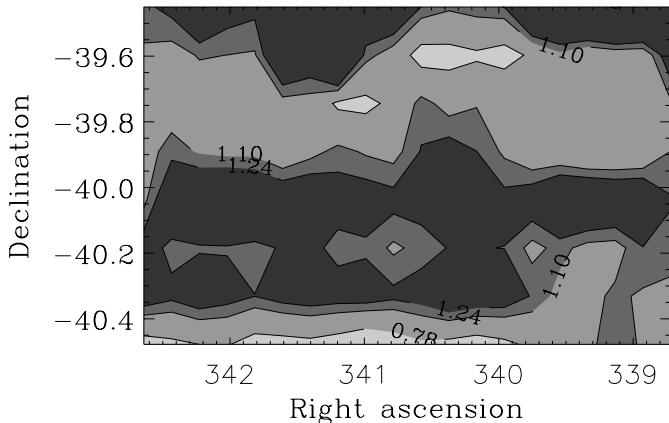


**Fig. 7.** Two-dimensional distribution of the seeing as measured on the *I*-band images for patch A for all the accepted even frames. Contours refer to 25, 50 and 75 percentiles of the distribution

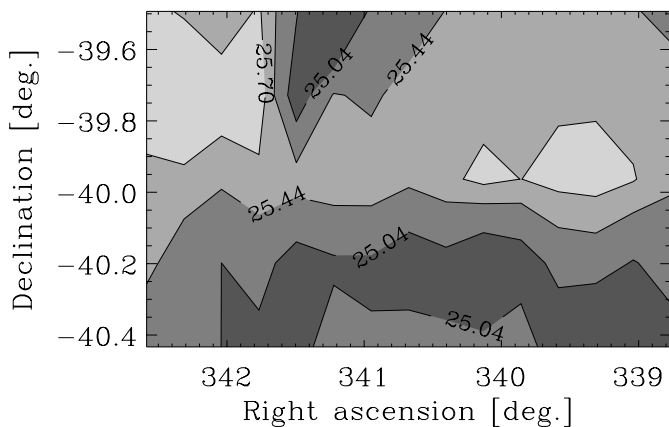


**Fig. 8.** Two-dimensional distribution of the computed  $1\sigma$  limiting isophote for the accepted even frames for patch A. Contours refer to 25, 50 and 75 percentiles of the distribution

between the results of the two algorithms shows that, while both lead to comparable results, the KSB software provides more robust results than SExtractor (Fig. 9). It is, however, considerably slower than SExtractor, and for the time being it is run in parallel to the main pipeline, just for diagnostic purposes.

The typical structure of the anisotropy of the EMMI PSF is shown in the upper left panel of Fig. 10, which displays the polarization vector for stellar images in a frame with a seeing of about 1 arcsec. As can be seen the anisotropy shows a complex structure and has a mean amplitude of  $\sim 6\%$  (lower left panel). However, the variation of the anisotropy is well represented by a second-order polynomial. Application of this correction leads to the small random residuals (rms  $\sim 2\%$ ) shown in the right panels of Fig. 10. Tests have also shown that the number of stars in the images of patch A is on average  $\sim 40$ . This number is sufficient to allow this correction to be computed even for typical survey frames.

More importantly, the EMMI images show a systematic increase in the size of the PSF along the *y*-direction of the CCD, while none is seen in the *x*-direction (Fig. 11). The difference between the size in the lower part and the upper part of the images is typically 10% which, in principle, can affect the star/galaxy classification algorithm. This effect was caused by the misalignment between the primary and secondary NTT mirrors. Recently, the mirrors have been realigned and a great improvement of the image quality is expected for the observations of patch D.

Since there were reports (Erben 1996) of problems in the optics of EMMI before its refurbishing, for comparison EMMI data from 1996 (Villumsen et al. 1998) and test data taken in April 1997 have also been analyzed. The PSF anisotropy map derived from images from 1996 showed erratic behavior even for consecutive exposures taken 10 minutes apart. By contrast, EIS images using the refurbished EMMI have proven to be quite stable. In fact, under similar observing conditions, the PSF anisotropy shows no strong time-dependent variations, as can be seen in Fig. 12 which displays nine consecutive frames of an EIS OB. This stability implies that the strong optical anisotropy can usually be corrected for.

The continuous monitoring of the EMMI PSF over an extended period of time will provide valuable information in order to better understand all the potential sources that may contribute to the anisotropy such as the telescope tracking and pointing as well as environmental effects. Even if this exercise proves to be of limited use for EIS, the implementation of these tools may be of great value for future surveys.

### 3.6. EIS database

A survey project like EIS collects a large number of science and calibration frames under varying conditions and produces a wealth of intermediate calibration parameters, catalogs and images. This multi-step process needs accurate monitoring as well as traceback facilities to control the progress and steer the survey as a whole. EIS is using a relational database consisting of several tables, which have been implemented in the course of the ongoing survey.

There are tables dedicated to storing parameters related to the observations such as: 1) FITS keywords for all images delivered by the ESO Archive to the EIS data reduction group; 2) Additional keywords for different types of images which include survey frames (tiles), photometric standards, astrometric reference frames, bias, flat-fields and darks; 3) extinction data observed routinely by the Swiss telescope and delivered by the Geneva Observatory.

Another set of tables are used to control and store the results of the photometric calibration process including: 1) additional parameters of the frames of photometric

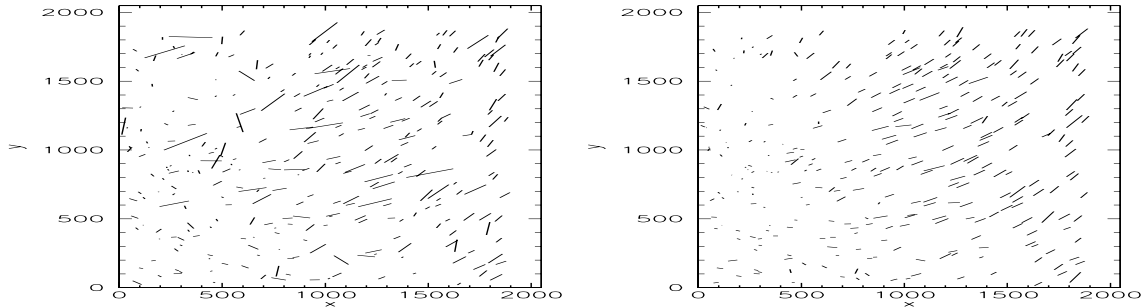


**Fig. 9.** Comparison of SExtractor and KSB shapes for stellar objects: The left panel shows the anisotropy structure as measured by SExtractor, while the right panel as measured by the KSB algorithm for the same stars

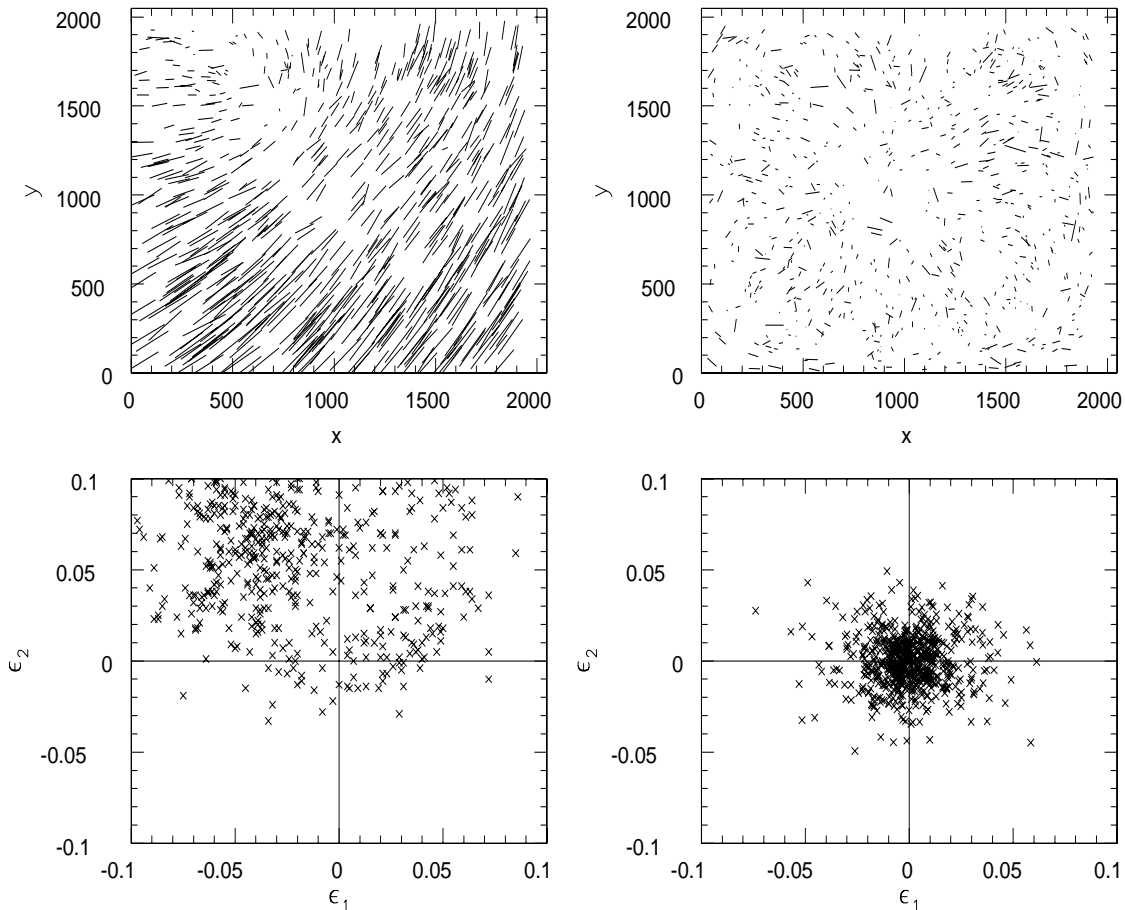


**Fig. 10.** A typical pattern of the PSF anisotropy (upper left) and components of the polarization vector (lower left) for an EMMI *I*-band frame (1 arcsec seeing). Also shown are the spatial distribution (upper right) and components of the polarization vector (lower right) after polynomial correction, as described in the text

standards; 2) information and results from different reduction runs of the photometric calibration data on a frame by frame basis; 3) data for photometric and spectrophotometric standards, combining results from the literature and from the reduction of the calibration frames on a star by star basis.

Finally, there are tables that: 1) store basic information about the nights in which EIS observations have been carried out; 2) control and monitor the processing of the

survey data; 3) store information about the coadded sections and the catalogs produced by the pipeline.

All these tables are related by common keys and the underlying commercial database engine used (Sybase) provides a powerful SQL dialect to manage and retrieve the stored data. Even though the EIS-DB is far from complete, its implementation is important as one can take full advantage of the available DB engine to retrieve key information about the survey, to control the processing and to provide a variety of statistics that can be used to fully

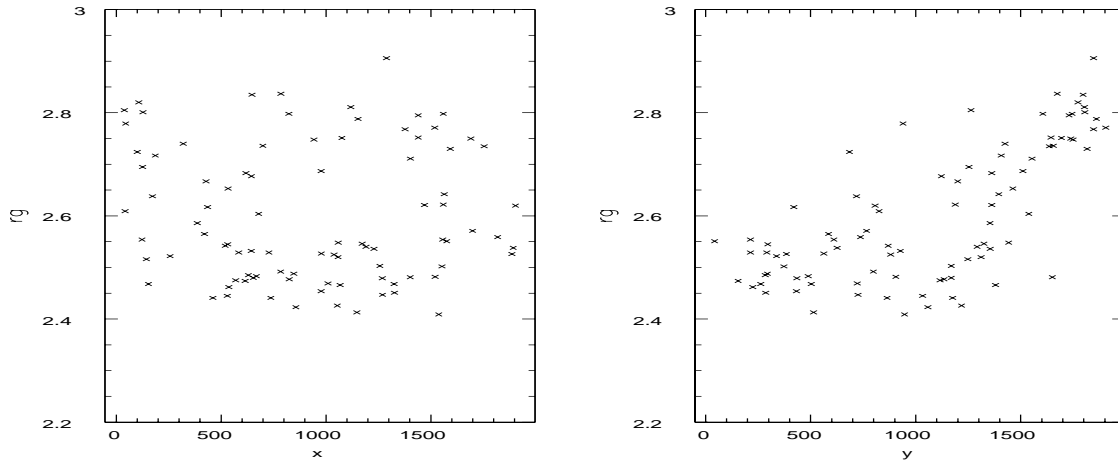


**Fig. 11.** Variation of the size of the PSF along the  $x$ -axis (left panel) and  $y$ -axis (right panel) of the CCD on EMMI. Note the increase in size near the top edge of the CCD. The quantity  $rg$  is the size of the stellar images as determined by the KSB algorithm. The image from which this result was derived has a seeing of  $\sim 1$  arcsec

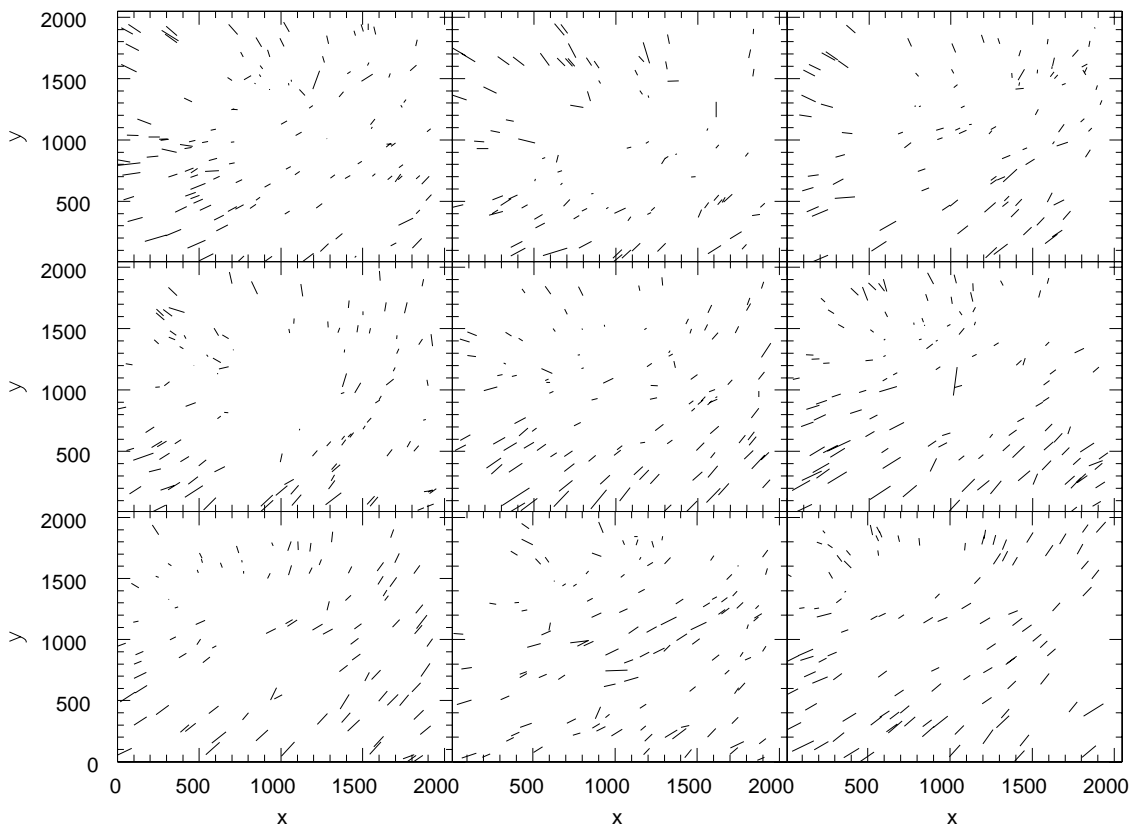


**Fig. 12.** Nine consecutive EIS images showing the stability of the PSF anisotropy with time

characterize it. A full description of the EIS database will be presented elsewhere (Deul et al. 1998).

### 3.7. Weighting and flagging

#### 3.7.1. Rationale

Because of the small number of EIS frames entering coaddition at a given position in the sky (typically two frames),

defects and other undesired features cannot be rejected through robust combination such as  $\sigma$ -clipping or by taking the mode of a histogram. In addition, two frames covering the same area in the sky can be observed at different epochs with very different seeing. Therefore, artifacts need to be identified on the individual images themselves, and discarded from coaddition. This can be achieved by creating maps of bad pixels.

This approach has been expanded to a more general one, which is the handling, throughout the pipeline, of a set of weight- and flag-maps associated with each science frame. Weight-maps carry the information on “how useful” a pixel is, while flag-maps tell why that is so. Using this approach, the image processing task does not need to interpret the flags and decide whether a given feature matters or not, which improves the modularity of the pipeline.

### 3.7.2. Implementation

The creation of weight- and flag-maps is left to the Weight Watcher program (see “<http://www.eso.org/eis>”). Several images enter into the creation of the weight and flag-map associated to each science frame. A gain-map — which is essentially a flatfield where the differences in electronic gains between the two read-out ports have been compensated — provides a basic weight-map. It is multiplied by a hand-made binary mask where regions with very strong vignetting (gain drop larger than 70%) and a  $\approx 30'' \times 30''$  CCD coating defect are set to zero and flagged. Bad columns stand out clearly in bias frames. Affected pixels are detected with a simple thresholding, marked accordingly in the flag-map, and again set to zero in the weight-map. A thresholding suffices to identify saturated pixels on science frames. These various steps are shown in Fig. 13.

### 3.7.3. Identification of electronic artifacts

Glitches cannot be identified as easily. Those include cosmic ray impacts, “bad” pixels and, occasionally, non-saturated features induced by the intense saturation caused by very bright stars in the field of view. Instead of designing a fine-tuned, classical algorithm to do the job, a new technique has been applied based on neural networks, a kind of “artificial retina”. The details of this “retina” are described elsewhere (Bertin 1999), but it suffices to say here that it acts as a non-linear filter whose characteristics are set through machine-learning on a set of examples. The learning is conducted on pairs of images: one is the input image, the other is a “model”, which is what one would like the input image to look like after filtering.

For the detection of glitches, a set of typical EIS images was used as input images, reflecting different seeing and S/N conditions (but putting stronger emphasis on good seeing images). Dark exposures containing almost nothing but read-out noise, cosmic-ray impacts and bad pixels were compiled. To these images a selection of more typical features, induced by saturation, were added. These “artifact images” were then used as the model images, and were also added to the simulations to produce the input images. The first EIS images used as input already contain unidentified cosmic-rays, producing ambiguity in the

learning. Thus the process was done iteratively (3 iterations), using images where the remaining obvious features are identified with a retina from a previous learning, and discarded. An example of a retina-filtered image is shown in Fig. 14.

A crude estimate (through visual inspection) of the success rate in the identification of pixels affected by glitches is  $\sim 95\%$ . The remaining 5% originate primarily from the tails of cosmic-ray impacts which are difficult to discriminate from underlying objects. The spurious detections induced by these residuals are, however, easily filtered out because of the large fraction of flagged pixels they contain (see Sect. 5.2).

### 3.7.4. Other artifacts

Unfortunately, there are other unwanted features that cannot be easily identified as such automatically: optical ghosts and satellite/asteroid trails. At this stage of the pipeline, obvious defects of this kind were identified through systematic visual inspection of all science images (Sect. 3.3). The approximate limits of the features are stored as a polygonal description which allows Weight Watcher to flag the related pixels and put them to zero in the weight-map.

### 3.8. Astrometric calibration

To derive accurate world coordinates for the objects extracted from EIS frames both the pairing of extracted objects in overlap regions and pairing of extracted objects with a reference catalog (USNO-A1) are used.

The pairing information of extracted objects with the reference catalog is obtained by assuming that the image header information is correctly describing the pointing center (with an accuracy of 10% of the size of the image) and the pixel scale (within 10%). Using a pattern recognition technique, that allows for an unknown linear transformation, the pattern of extracted objects is matched with the pattern of reference stars. This results in corrections to the pointing center and pixel scale. Then applying these corrections the pairing between extracted objects in the overlap regions is performed.

Because the unit of measurement is a set of ten consecutive, overlapping frames in which the telescope is operating in a mechanically coherent manner (offset pointing, vs. preset pointing between sets of ten frames) this forms the basis for an astrometric solution. Independent pointing offsets are determined for each frame, while considering the focal scale and distortion parameters as constant or smoothly variable as a function of frame number in the set. The plate model is defined as the mapping between pixel space and normal coordinates (gnomonic projection about the field center). This mapping is a polynomial description

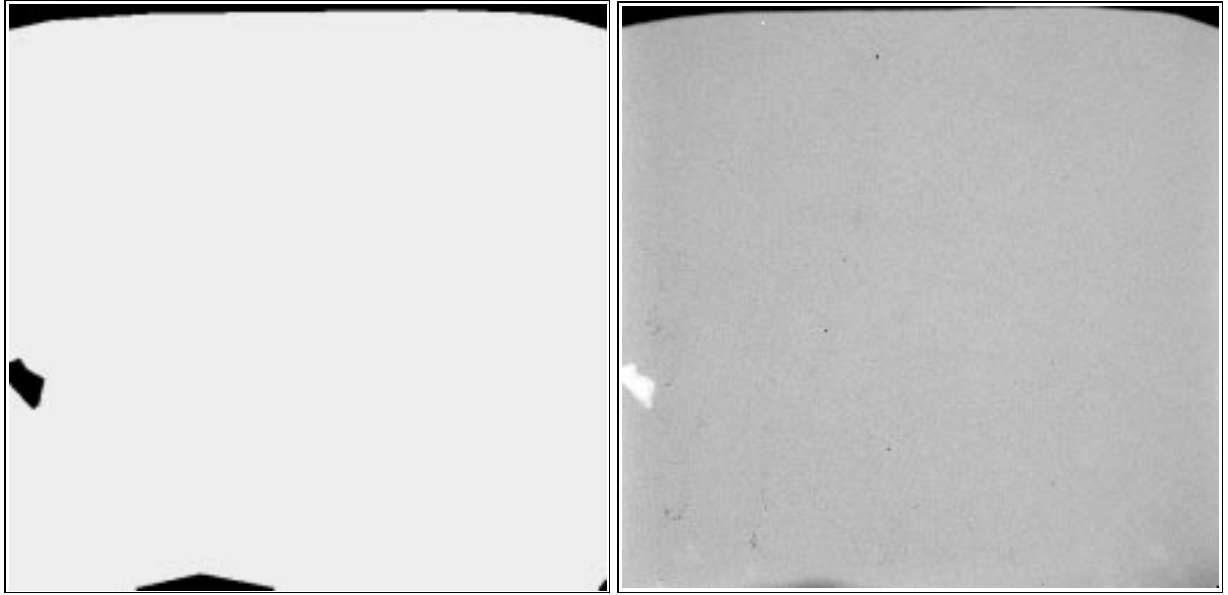


**Fig. 13.** Two components of the weight maps: the hand-drawn mask (left panel), which excludes strongly vignetted regions, and the gain map (right panel) obtained from the flatfield

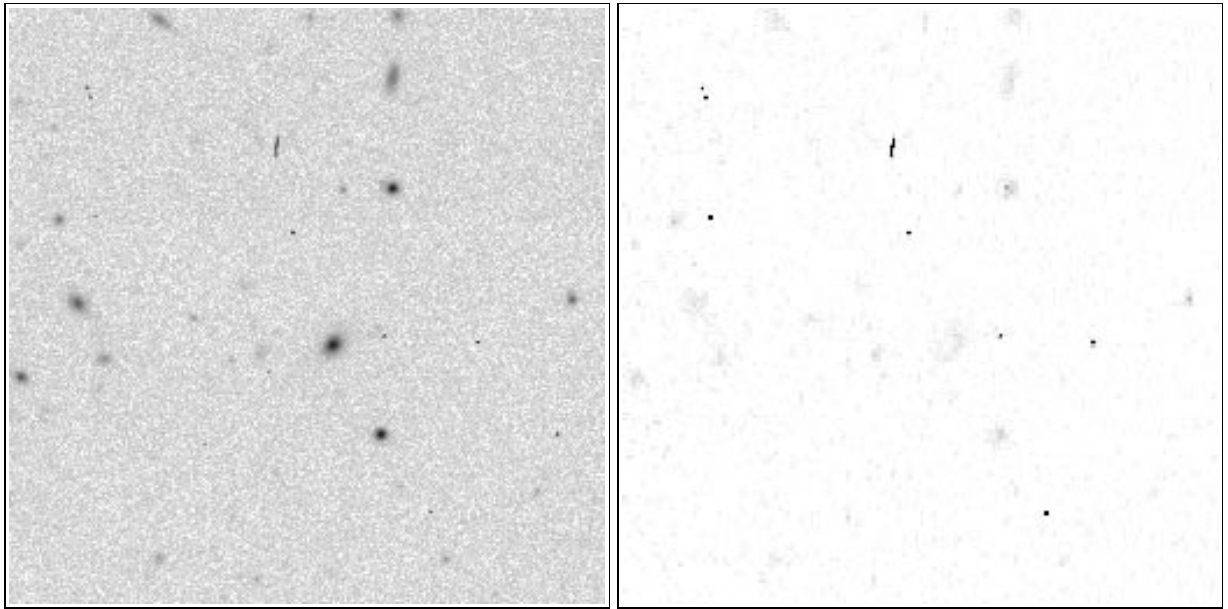


**Fig. 14.** *Left:* Part of an EIS image with very good seeing ( $FWHM = 0.54''$ ). *Right:* retina-filtered image of the same field, showing up cosmic-ray impacts. Both images with negative scale

for which the polynomial parameters are allowed to vary smoothly (Chebychev polynomial) with frame number in the set. Therefore, the mapping between  $(x, y)$  pixel space and  $(\zeta, \eta)$  allows for flexure and other mechanical deformation of the telescope while pointing.

Using pairing information, association of the source observed in several frames, and association of the extracted source with the reference catalog, a least squares solution is derived where these distances between the members of the pairs are simultaneously minimized. Weighting is done in accordance with the positional accuracy of the input

data. The source extraction accuracy rms is 0.03 arcsec, while the reference has an rms of order 0.3 arcsec. The astrometric least squares solution is done in an iterative way. Because associations have to be derived before any astrometric calibration has been done, erroneous pairings may occur. A Kappa-Sigma clipping technique allows for discarding the large distance excursions (probable erroneous pairings) between the iterations.

From the astrometric solution it is found that distortion of the pixel-scale is  $\lesssim 0.5\%$  and the accuracy of the relative astrometry is  $\sim 0.03$  arcsec.

### 3.9. Photometric calibration

#### 3.9.1. Method

Deriving a coherent photometric system for observations done in both photometric and non-photometric conditions is a challenge handled in EIS through a stepwise procedure.

The first step is to derive the relative photometry among frames in an overlapping set. In contrast to what is done for the astrometric calibration, all overlaps among frames in a contiguous sky area are used. Using the overlap pairing information, an estimate for the total extinction difference between frames can be computed. This can be expressed in terms of a relative zero-point, which by definition, includes the effects of airmass and extinction. To limit the magnitude difference calculation to reliable measurements, a selection of input pairs is made based on the signal-to-noise ratio, maximum allowed magnitude difference between members of a pair, and limiting magnitudes for the brightest and faintest usable pairs. Because a set of frames will have multiple overlaps, the number of data points (frame-to-frame magnitude differences) will be over-determined with respect to the number of frames. Therefore, the relative zero-point for each frame can be derived simultaneously in a least squares sense. Weighting is applied based on the number of extracted objects and their fluxes. The solution is computed in an iterative fashion. Estimated frame-based zero-points from a previous iteration are applied to the magnitudes and new sets of pairs are selected, rejecting extraneous pairs. The process stops when no new rejections are made between iterations. The internal accuracy of the derived photometric solution is  $\lesssim 0.005$  mag.

The second step involves correcting possible systematic photometric errors, and deriving an absolute zero-point. Systematic errors are introduced by incorrect flat-fielding (stray-light, pixel-scale variations, gain changes between read-out ports) or variation of image quality. The latter has, however, been minimized by adopting an appropriate photometric estimator (Sect. 5.1.2). The correction for these systematic errors can be made by using external information, such as pointed measurements from other telescopes, and/or absolute zero-points from EIS measurements of Landolt standards, which are used to anchor a global photometric solution. As long as these observations cover the patch uniformly, systematic zero-point errors can be corrected by a weighted least-square fit of a low-order polynomial to the difference between the relative zero-point derived from the previous step and the external pointed measurements. This general procedure will be adopted in the final version of the EIS data.

#### 3.9.2. Calibration of patch A

In this preliminary release, the zero-point calibration of patch A was determined to be simply an offset derived from a weighted average of the zero-points of the available anchors. For patch A, the available anchor candidates are: the 2.2 m data, the 0.9 m data and the EIS tiles taken during photometric nights. Given the fringing problems detected with the 2.2 m data, the latter have, for the time being, been discarded. For patch A, five nights were observed under photometric conditions. This represents about one hundred tiles, covering a wide range in declination (Fig. 5).

There are some indications for a small zero-point gradient in right ascension ( $\sim 0.02$  mag/deg), in agreement with the uncertainties of the flat-fields ( $\sim 0.002$  mag). By contrast, the behavior along the north-south direction is much less well determined, as it relies on calibrations generally carried out in different nights. With the current calibrations, however, the systematic trend is estimated to be  $\lesssim 0.2$  mag peak-to-peak, which is the amplitude of the measured zeropoint differences and is more likely to be of order 0.02 mag peak-to-peak, which is the extrapolation of the flat-field uncertainties.

The DENIS strip could have been a perfect data set to constrain the homogeneity of the zero-point in declination. However, careful examination of the DENIS standards revealed a significant variation in the zero-points for the night when this strip was observed, preventing its use to constrain possible gradients in declination of the EIS data. Note that another strip crossing the surveyed area has also been observed and an attempt will be made to retrieve it from the DENIS consortium before the final release of the EIS data.

#### 3.10. Coaddition

Coaddition serves three main purposes: it increases the depth of the final images; it allows the suppression of artifacts which are present on some images (such as cosmic-ray hits); and it allows the creation of a “super-image” of arbitrary size to facilitate studies which would be affected by the presence of the edges of the individual frames.

A general coaddition program had been developed from the “drizzle” method originally created to handle HST images (Fruchter & Hook 1997; Hook & Fruchter 1997). The inputs for each coaddition operation are the survey frame and a weight map which, as mentioned above, gives weight 0 to the bad pixels. The corner positions of each input pixel are transformed, using the astrometric solution generated by the pipeline, first into equatorial sky positions and then onto pixel positions in the output super-image. The conic equal-area sky projection is used for the super-image as it minimizes distortion of object shapes and areas. To ease manipulation and

display the super-images are normally stored as sets of contiguous  $4096 \times 4096$  pixel sections.

To compute the super-image pixel values, the corners of each input pixel are projected onto the output pixel grid of the super-image to determine the overlap area. The data value from the input image is then averaged with the current values in the output super-image using weighting which is derived by combining the weight of the input, the weight of the current output pixel and the overlap area. The method reconstructs a map of the surface intensity of the sky as well as an output weight map which gives a measure of the statistical significance of each pixel value. A third output image, the “context map” encodes which of the inputs were coadded at a given pixel of the output so that properties of the super-image at that point, such as PSF-size, can be reconstructed during subsequent analysis. The values in the context-map provide pointers to a list which is dynamically generated and updated during coaddition. This is a table of the unique image identifiers for a specified context as well as the number of input images and the number of pixels having a given context value.

#### 4. Data products

The EIS pipeline produces a wide array of intermediate products, both images and catalogs, as well as a large set of logs, reports and diagnostics. A full description of these products is beyond the scope of the present paper and will be presented elsewhere.

In this preliminary release the following data are publicly available at “<http://www.eso.org/eis>”:

**Single frames:** sky-subtracted, fully calibrated frames, in integer format. They can be retrieved at the above WWW address, where a request form will be available. The requests will be handled by the Science Archive Group. Note that the calibrated images being distributed have not been corrected for cosmetic defects. In particular, they contain bad columns, cosmic rays and the vignetted region at the top and bottom edges of the frames. However, all of these artifacts have been taken into account in the production of the object catalogs and the information available in them allows one to filter out affected objects. To provide approximate astrometric information the CD-matrix convention (as given in the Users Guide for the Flexible Image Transport System 1997 version 4) has been adopted to describe the world-coordinate system, and included in the FITS header of each frame. Even though this is in general a reasonable approximation it is not appropriate to account for the distortions of the frames. Therefore, when object catalogs are overlaid onto the images some residuals are visible, especially at the corners of the images. The photometric zero-point for each frame after the absolute photometric calibration of the frame appears in the header of the image. A full

description of the EIS specific keywords can be found at “<http://www.eso.org/eis>”.

**Coadded sections:** sky-subtracted, fully processed (see above) sections of the coadded image. These sections are mapped using the conic equal area (COE) projection (Greisen & Calabretta 1996). Note that this projection is not handled by all display-tools but has already been implemented in the ESO SkyCat. The available images are lossy compressed using an HCOMPRESS library originally written by White (1992) for the STScI. The coadded sections have been compressed using a very high compression scale of 200. In addition to the compression, the images are re-sampled by a factor of 0.5 in both directions using the re-sampling code developed by Devillard (1997). The size of the original images is 67 MB, whereas that of the compressed and re-sampled images is about 150 kB. These sections are handled by an on-line server, similar to that available for the Digitized Sky Survey (DSS). A preliminary object catalog, containing only position and shape information is also available on the on-line server. For the display of the sections and the catalog SkyCat can be used as an interface.

**Low-resolution coadded image:** sky-subtracted, fully processed coadded image. This image is meant to give a general overview of the whole patch and it has been produced by re-binning (3 arcsec pixel size) and pasting together the sections. This is a standard output of the pipeline. This image (~25 Mb) can be retrieved at the same web page as above.

**Single frame catalogs:** Object catalogs associated with each single frame. A full description of the parameters available is presented below. The name convention of the catalogs is based on that of the EIS tiles  $A_{i,j}$  (see Sect. 2). The catalogs are in binary FITS table format.

Note that the coadded sections and image currently available are not suited for astronomical reduction because of the varying noise properties and compression, but are useful for proposal preparation and comparison with EIS catalogs or other data sets.

The main difference between the current release and the final release of the EIS data is that the latter will also include the coadded image and the auxiliary weight and context maps, as well as the final object catalog which will contain information about the context within which a given object has been identified. The inclusion of the context information into the catalog extracted from the coadded image is currently underway.

#### 5. Object catalogs

##### 5.1. Source detection and photometry

In a survey like the EIS, where a large variety of astronomical — and non-astronomical! — objects of all kinds can be detected and measured over wide areas, one cannot avoid

making choices. In the case of EIS, the priority is the detection of objects such as faint stars and galaxies. Brighter objects are generally saturated and/or already cataloged. The source extraction is performed with a new version of the SExtractor software (Bertin & Arnouts 1996) that can be retrieved from “<http://www/eso.org/eis>”. SExtractor is optimized for large scale imaging survey fields with low to moderate source density, and is therefore perfectly suited to EIS. The processing is done in 3 steps: detection, measurement, and classification, which are briefly described for the single image process.

### 5.1.1. Detection

For each image, the detection process in SExtractor begins with the determination of a smooth background map. This is done by computing the modes of histograms built from meshes of  $64 \times 64$  pixels, corresponding to  $\approx 17$  arcsec. This relatively small scale was chosen in order to facilitate the detection of faint objects on top of the strong gradients encountered near the many bright stars in the survey (3 out of the 4 EIS-wide fields are located at moderate galactic latitude). This produces a lower resolution image ( $32 \times 32$ ) of the background (hereafter referred to as miniback). This miniback is median-filtered using a  $3 \times 3$  box-car, to avoid the contamination of the background map by isolated, extended objects. The median filtering also helps to reduce photometric bias for bright, “large” galaxies, to a negligible fraction up to scales  $\gtrsim 40''$ , which correspond to  $I \lesssim 18$ . A full-resolution background map is obtained by interpolating the smoothed miniback pixels, using a bicubic-spline, and is subtracted from the science image.

Background-subtracted images are then filtered before being thresholded, to reduce the contribution of noise on spatial scales of the image where it is dominant. The median seeing ( $FWHM$ ) of EIS images as a whole is about 0.9 arcsec, a little more than 3 pixels. The data are filtered by convolving with a slightly larger, constant, Gaussian profile with  $FWHM = 4$  pixels. Although the choice of a convolution kernel with constant  $FWHM$  may not always be optimum (the seeing may vary by as much as a factor of 3), the impact on detectability is, however, fairly small (see Irwin 1985). On the other hand, it has the advantage of requiring no change of the relative detection threshold. It also simplifies the comparison with the coadded-image catalog, for which the convolution kernel is also fixed.

The detection threshold,  $k\sigma$ , used in SExtractor is expressed in units of the standard deviation  $\sigma$  of the background noise. For single images  $k = 0.6$  is used, which corresponds to a typical limiting surface brightness  $\mu_I \sim 24 - 24.5$  mag/arcsec<sup>2</sup>. The new SExtractor allows this noise-level to be set independently for each pixel  $i$ , using a weight-map  $w_i$  (Sect. 3.7), which is internally converted to a relative variance:  $\sigma_i^2 \propto w_i^{-1}$ . The variable

detection threshold is also used for deciding if a faint detection lying close to a bright object is likely to be spurious or not.

Some pixels are assigned a null weight by Weight Watcher, because they are unreliable: gain too low, charge bleeding, cosmic-ray, etc. The detection routine cannot simply ignore such pixels, because some objects, like those falling on bad columns or charge bleeding features, would be either truncated or split into two. A crude interpolation of bad pixels overcomes this problem. Unfortunately, interpolation creates correlated patterns which are sometimes detected at the very low thresholds applied in the EIS, but as these zones are flagged, they are easily filtered out in the final catalog.

### 5.1.2. Measurement

Basic positional and shape parameters are computed for each detection on the convolved image. These include the barycenter, major, minor axes and position angle derived from the second-order moments of the light distribution and the associated error-estimates, which take into account the weighting of each pixel. The photometry is performed on the un-convolved, un-interpolated image. Photometric parameters measured on the images include isophotal magnitudes, fixed-disk aperture magnitudes with diameters ranging from 2.7 to 14 arcsec (14 arcsec is the typical “Landolt aperture”), and SExtractor’s estimate of “total” magnitude: MAG\_AUTO. The latter is a Kron-like elliptical aperture magnitude. It is computed in a way similar to that proposed by Kron (1980), except that the aperture is required to be elliptical, with aspect-ratio and position angles derived from the second-order moments. For the measurement of magnitudes, pixels with zero-weight and those associated with the isophotal domain of some neighbor are handled in a special way by the new SExtractor: when possible, they are replaced by the value of the pixel symmetrical to the current one, with respect to the barycenter of the object. Although this simple algorithm is certainly crude, it proves to yield fairly robust results and replaces advantageously the MAG\_BEST estimator used in the old SExtractor (Bertin & Arnouts 1996). One particular aspect of EIS is the large variation in the seeing from frame to frame. Simulating EIS images of point sources under different observing conditions, it is found that the MAG\_AUTO magnitudes are fairly robust with respect to seeing variations: systematics of only  $\approx 1\%$  peak-to-peak are expected for the bright stars used in the photometric solution.

### 5.1.3. Classification

The standard SExtractor star/galaxy classifier is a multilayered back-propagation neural-network fed with

isophotal areas and the peak intensity of the profile. The classifier was trained with simulated ground-based, seeing-dominated, optical images. It will therefore perform well on images close to the conditions met in the original simulations. This is so for EIS images in patch A, but it is no longer the case for other patches, where very good seeing and strong optical distortions yield significantly elongated and skewed stellar profiles, varying over the frame. A new, more general, star/galaxy separation scheme is therefore needed for these fields, and is currently being implemented in SExtractor.

The current classifier returns a “stellarity index” between 0 and 1. A value close to 0 means the object is extended (galaxy), while a value close to 1 indicates a point-source (star). It can be shown that the neural network output is approximately the probability that an object is a point-source. This is only valid for a sample of profiles which would be drawn from the same parent population as the training set. Because the neural classifier is a finely tuned system, these conditions are almost never met with real images, and care has to be taken when interpreting the stellarity index. Nevertheless, it is fair to adopt a stellarity index value of 0.5 as a default limit between point-sources and elongated objects. At faint levels ( $I \gtrsim 21$ ), star/galaxy separation begins to break down for frames obtained under the least favorable seeing conditions in patch A. A clump begins to form around a stellarity index of 0.5, indicating that the algorithm cannot provide a reliable classification for most objects.

In the discussion below two values of the stellarity index are adopted to separate stars and galaxies: the conservative value of 0.5, which tends to favor more complete star catalogs, and a value of 0.75, which assumes that beyond the classification limit galaxies largely outnumber stars.

### 5.2. Single frame catalogs

The most basic catalogs are the single frame catalogs which are generated by SExtractor. These are produced by default by the pipeline in a two-step process. First, SExtractor is run with a high threshold to identify stars and determine a characteristic value of the *FWHM* for each frame. This value of the *FWHM* is then used as input to a second run of SExtractor with a low-threshold for detection which also provides the classification of the detected objects by computing the stellarity-index.

During the extraction SExtractor sets several flags to describe any anomalies encountered. The meanings of these flags,  $f_s$ , are summarized in Table 2. Information available in the flag-maps generated by the Weight Watcher program are also propagated to the catalog. Flags are set to indicate that a given object is affected by bad pixels in the CCD-chip or by artifacts in the image that have been marked either by the artificial

**Table 2.** Description of SExtractor flags ( $f_s$ )

Value	Description
1	The object has neighbors bright and close enough to significantly bias the MAG_AUTO photometry
2	The object was originally blended with another one
4	At least one pixel of the object is saturated
8	The object is truncated (too close an image boundary)
16	Object’s aperture data are incomplete or corrupted
32	Object’s isophotal data are incomplete or corrupted
64	A memory overflow occurred during de-blending
128	A memory overflow occurred during extraction

**Table 3.** Description of Weight Watcher flags ( $f_w$ )

Value	Description
1	The object contains pixels that were marked in the image mask
2	The object contains pixels with a deviating gain
4	The object contains pixels with a deviating bias
8	The artificial retina detected a cosmic ray hit within the object
16	The object contains saturated pixels
32	The object was masked out during eye-balling

retina or by the polygon-masking during visual inspection (Sect. 5.4). Table 3 summarizes the meaning of the flags in the catalog set from the information contained in the flag-maps,  $f_w$ .

The contents of the catalogs include: J2000.0 right ascension and declination,  $x$  and  $y$  coordinates in the chip; total magnitude (MAG\_AUTO) and error; major and minor axes; position angle; stellarity index; SExtractor flag  $f_s$  (see Table 2); Weight Watcher flag  $f_w$  (see Table 3); total number of pixels above the analysis threshold ( $n_{\text{pix}}$ ); total number of pixels that are flagged by Weight Watcher ( $n_{\text{flag}}$ ). Further information can be found at “<http://www.eso.org/eis>”.

### 5.3. Derived catalogs

During the processing of a patch through the pipeline the single frame catalogs are merged together into a “patch” catalog which contains information of all objects identified in the individual frames. Note that objects may have multiple entries if they are in overlapping frames. From this patch catalog several single entry catalogs may be derived, for instance, the even/odd catalogs containing all objects detected in the even/odd frames. Objects detected in more than one frame are identified to produce a single-entry in the final catalog, choosing the parameters as determined from the best-seeing image. Objects in regions of overlap

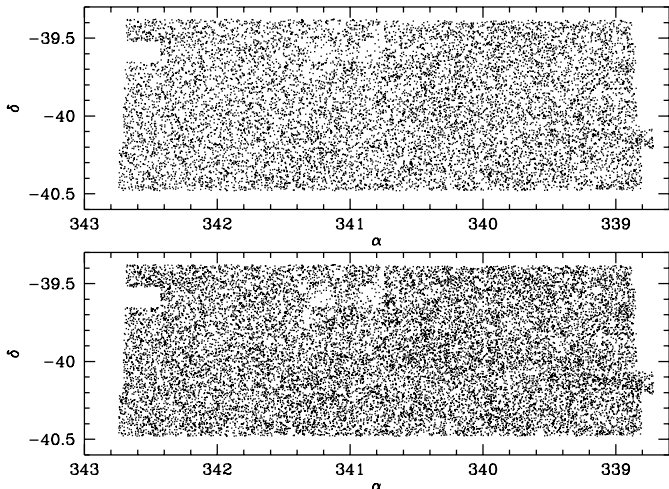


**Fig. 15.** Distribution of stars detected in the even frames covering patch A at magnitudes brighter than  $I = 20$  (12355 objects, upper panel) and  $I = 21$  (18529, lower panel). Objects with a stellarity index  $> 0.5$  were classified as stars. Note the two bad frames in the upper part of the patch, yielding nearly empty regions. As pointed out in the text this region is usually discarded from the analysis

are paired whenever the barycenter of the smallest falls within an ellipse twice the size of the object ellipse of the larger one. Details on this procedure will be presented elsewhere (Deul et al. 1999).

From the flag information available in the single-entry catalog, *filtered* catalogs can be produced for analysis purposes (see Sect. 6). The filtering is required to eliminate truncated objects and objects with a significant number of pixels affected by cosemics and/or other artifacts. Objects with the following characteristics are discarded:  $f_s \geq 8$  or  $nflag/npix \geq 0.1$ , where  $f_s$  is the SExtractor flag,  $npix$  the number of pixels above the analysis threshold and  $nflag$  the number of pixels flagged by Weight Watcher. The two-dimensional distribution of stars and galaxies from the resulting catalog are shown in Figs. 15 and 16, for different limiting magnitudes.

#### 5.4. Visual inspection

The visual inspection of the catalogs was done using the new version of ESO SkyCat which also provides the possibility of accessing the EIS catalogs through the on-line server. Further information on the SkyCat setup can be found at “<http://www.eso.org/eis>”. This setup interprets the parameters and flags available in the EIS catalogs. To distinguish between the different object classes and flags, the following plot symbols and colors have been used:

- White (black) circles - stellarity index  $\geq 0.75$  and  $f_s < 4$ .
- Red circles - stellarity index  $\geq 0.75$  and  $f_s \geq 4$ .
- Yellow ellipses - stellarity index  $< 0.75$  and  $f_s < 4$ .

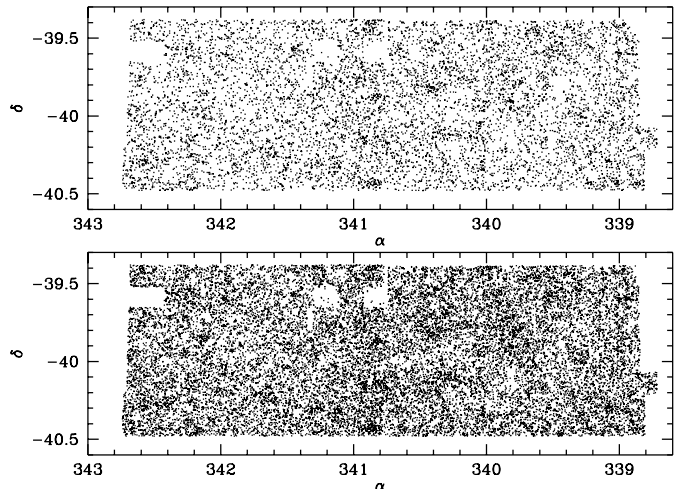


**Fig. 16.** Same as in previous figure showing the distribution of 9006 (upper panel) and 23129 (lower panel) galaxies for the same two limiting magnitudes as in Fig. 15. Again note the empty regions in the upper part of the patch caused by bad frames

- Red crosses - stellarity index  $< 0.75$  and  $f_s \geq 4$ .

This tool has been extensively used to fine-tune the configuration parameters used by SExtractor and Weight Watcher as well as to inspect the performance of the filtering of the catalogs (see Sect. 5.3). Users of the catalogs should be aware of the following features:

- Many spurious objects are present near or within masked regions. This is most noticeable along the frame border, affected by vignetting, and along the bad pixel column. Real objects close to the masked regions may also go undetected.
- The largest cosmic rays can be classified as objects.
- Spurious objects can be found in presence of very bright stars.
- The de-blending can fail when one of the objects in a merged or very close pair, is much fainter than the other one (the faint object is included as part of the brighter). Failures can also occur for close objects of the same brightness when the seeing is bad or the PSF is elliptical.
- High surface brightness galaxies fainter than  $I \sim 21$  might be given a high value for the stellarity index (larger than 0.8 or even 0.9).

The visual inspection shows that, by adopting the filtering criteria described in the previous section, most of the spurious objects are appropriately removed.

#### 5.5. Uniformity of the detections

As a first check on the quality of the object catalogs produced by the pipeline it is important to examine the uniformity of the detections across the effective area (excluding the regions masked out) of the EMMI-frame.

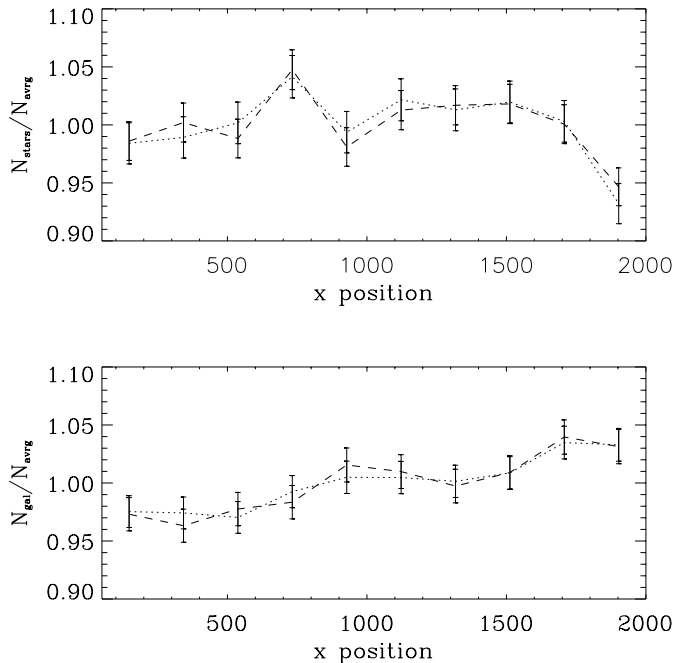


**Fig. 17.** The uniformity of the detections in the east-west direction. The top panel shows the detected stars brighter than  $I = 21$  for a stellerity index  $\geq 0.75$  (dotted line) and stellerity index  $\geq 0.5$  (dashed line). For fainter magnitudes the classification breaks down. The bottom panel shows the detected galaxies brighter than  $I = 21$  stellerity index  $< 0.75$  (dotted line) and stellerity index  $< 0.5$  (dashed line). It is seen that the star counts show a dip at the “right” edge of the chip, and a corresponding increase in the galaxy counts. This feature is attributed to the image distortions, see text for details

This is shown in Figs. 17 and 18, where the normalized average counts of stars and galaxies as a function of the east-west (Fig. 17) and north-south position (Fig. 18) on the chip are displayed. The upper panels show the star counts brighter than  $I = 21$ , which is the limiting magnitude for reliable classification in patch A as a whole. The lower panels show the galaxy counts to the same limiting magnitudes.

The overall uniformity of the detections at magnitudes  $I \leq 21$  is good. A small decrease in the number of stars is seen at the upper edge of the chip and is almost compensated by an increase in the galaxy counts. This behavior is likely to be due to misclassifications caused by the increase in size of the PSF as shown in Sect. 3.5.

### 5.6. Completeness and reliability

To verify the pointing of the telescope, a reference field has been observed before the start of each row (150 s) and, in some cases, the start of sub-rows (50 s). These exposures, which for patch A total 2250 s, were used to determine the offset required to compensate for the problems detected with the NTT pointing model. Using the EIS

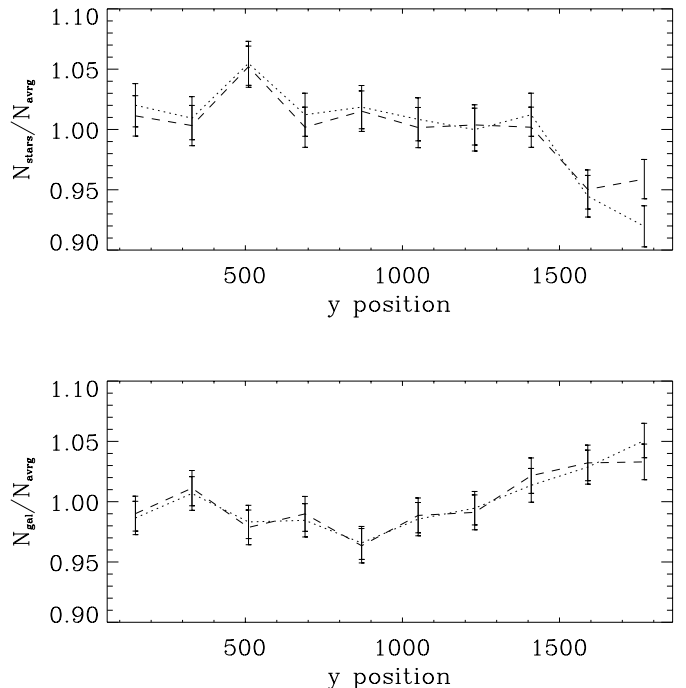


**Fig. 18.** As Fig. 17 but showing the detections in the north-south direction. Again at the “upper” edge of the chip we see a dip in the star counts and a corresponding increase in galaxy counts, which is due to the image distortions, see text for details

pipeline these images have been coadded and an object catalog was produced extending to fainter magnitudes. This catalog has been used to empirically determine the completeness of the detections in typical single-frame EIS catalogs. This was done by comparing the catalog produced from the coadded image of the reference field to the individual catalogs derived for the various exposures of that field. Since the limiting magnitude of the coadded image is much fainter than that of the single frames, one can assume that the coadded catalog is complete and that it is not significantly contaminated with false objects at least to the limiting magnitude of the single-frame catalogs. Keeping this in mind a match was made between all the objects in the coadded catalog and those found in the single-frame catalogs. The ratio between the number of paired objects and the total number of objects in the coadded catalog provides a measure of the differential completeness as a function of magnitude, which is shown in Fig. 19. The completeness defined in this way only measures the fraction of objects actually found, but does not tell anything about the reliability of their properties. It is seen from the figure that for objects of magnitude  $I \sim 23$  the completeness is  $\sim 80\%$ . At this magnitude the integrated completeness of the catalog is 94%. The completeness does not vary for seeing between 0.7 and 1.3 arcsec. For a seeing of 1.5 arcsec the 80% differential completeness limit is at  $I \sim 22$ .

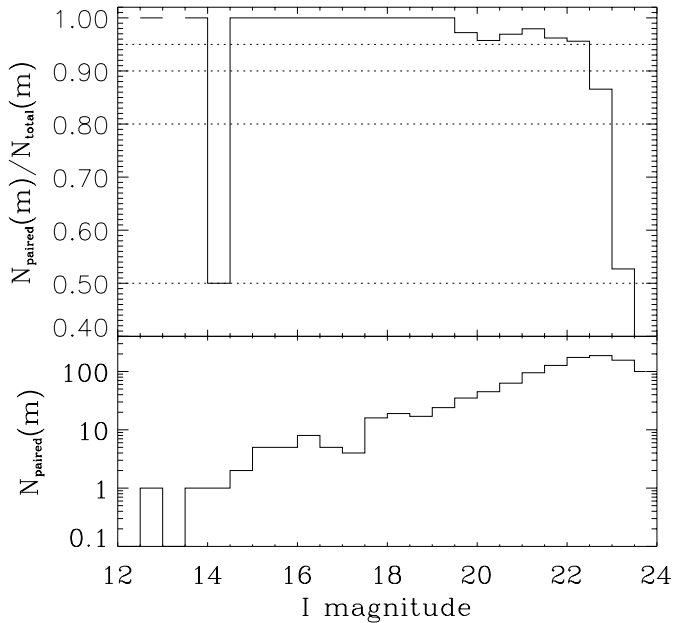


**Fig. 19.** Top panel: Completeness of the single-frame catalogs as determined from the comparison with the reference field. The plot shows the ratio between the number of objects found in both the coadded image and a single frame and objects found in the coadded image as a function of magnitude. The figure shows that at  $I \sim 23$  the single-frame catalogs are 80% complete. Bottom panel: The number of paired objects, to give an idea of the statistical errors in the comparison

The number of false detections can be estimated in a similar way. Figure 20 shows the ratio between objects that were found in a single-frame catalog but not in the coadded one and the total number of objects in the single-frame catalog. The figure is based on a comparison obtained using a single frame with a seeing of 1.07 arcsec, which is close to the median seeing of the observations for the patch. It is seen that at  $I \sim 22.5$  10% of the objects are false detections and 20% of the objects with magnitude  $I \sim 23$  are spurious. The integral fraction of spurious objects up to the limiting magnitude of  $I = 23$  is  $\sim 6\%$ .

### 5.7. Errors in magnitude and classification

A comparison between even and odd catalogs provides further useful information on the accuracy of the magnitudes and on the robustness of the classification as a function of magnitude. This comparison was done using a test region of 0.6 square degrees, with a median seeing of 0.95 arcsec. Using the same pairing procedure previously discussed, a catalog of paired objects in the test region was produced.

A lower limit estimate of the photometric errors can be obtained from the repeatability of the magnitudes of the paired objects. Figure 21 shows the magnitude difference of these objects as a function of magnitude. The standard deviation of the magnitude differences in the in-

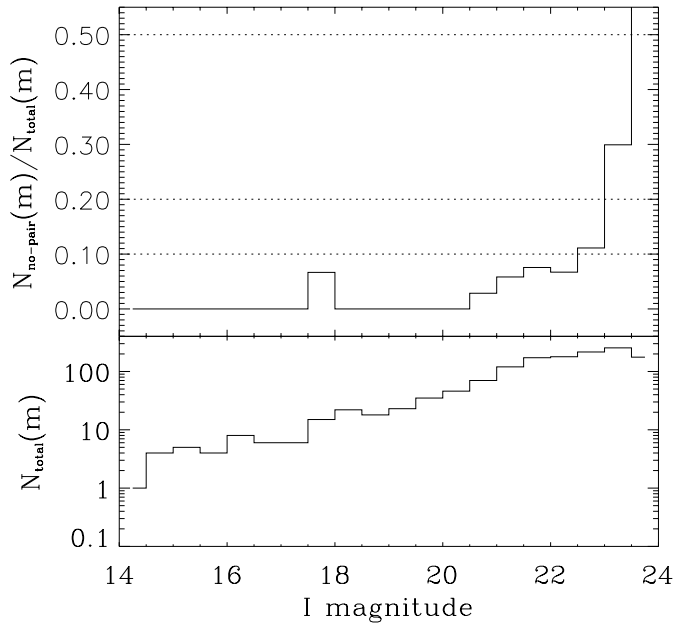


**Fig. 20.** Top panel: ratio of the number of objects found in a single-frame but not in the the coadded catalog of the reference field and total number of objects in the corresponding single-frame catalog. At  $I \sim 22.5$  there are 10% false objects and at  $I \sim 23$  there are 20% spurious detections. Bottom panel: total number counts in the single-frame catalog

terval  $16 < I < 20.5$  ranges between 0.02 and 0.1, reaching 0.3 at  $I \sim 23$ .

Figure 22 shows a comparison between the errors determined from the magnitude difference shown above (divided by  $\sqrt{2}$ ) and the SExtractor error estimates based on photon statistics. SExtractor provides reasonable error estimates over the interval of interest. At bright magnitudes photometric errors are dominated by effects such as flatfield errors, image quality, intrinsic stability of the MAG\_AUTO estimator and relative photometry.

For objects in the magnitude range  $16 < I < 21$  and adopting a stellarity index of 0.75 to separate stars and galaxies, about 5% of the objects have different classifications in the even and the odd catalogs. For magnitudes  $I \lesssim 16$  most objects are saturated and may be classified as galaxies. However, they can be found as having the flag  $f_w = 16$ , which has been used to exclude them from subsequent analysis.

## 6. Data evaluation

### 6.1. Galaxy and stellar counts

Since EIS observations were carried out under varying conditions, it is important to evaluate the degree of homogeneity of the final object catalogs. This can be done by examining, for instance, the number counts as a function of magnitude and comparing with earlier work.

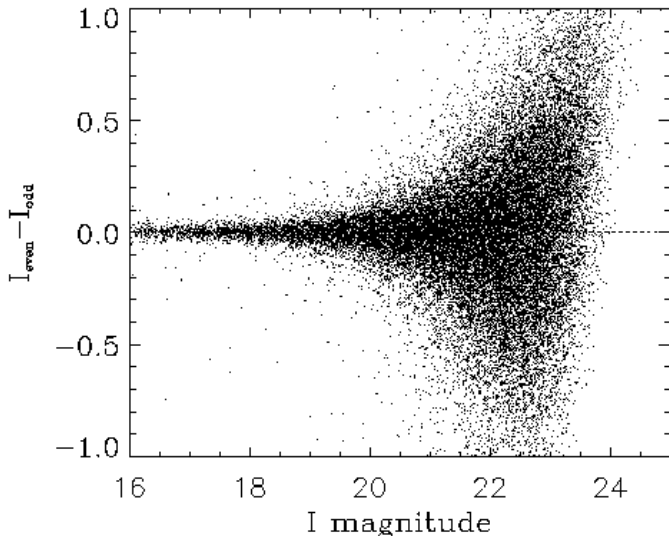


**Fig. 21.** The magnitude differences between detections in the even and odd catalogs as function of magnitude. At bright magnitudes the standard deviation varies between 0.03 mag and 0.1 mag, reaching 0.4 mag at  $I \sim 23$

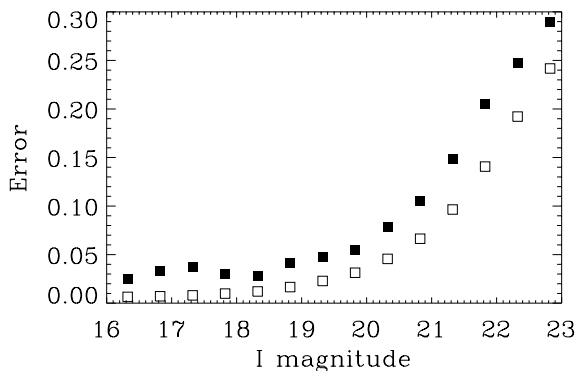


**Fig. 22.** Comparison between the standard deviation of the EIS-magnitude differences (filled squares) and the magnitude errors estimated by SExtractor (open squares) as function of magnitude

To evaluate the variation in the number counts due to the varying observing conditions, the area of patch A covered by both even and odd tiles, comprising 3 square degrees, has been divided into six subregions, each having an area of 0.5 square degrees. Note that these areas cover most of patch A including highly incomplete regions (see Fig. 16). The number counts for each subregion are computed and the mean is shown in Fig. 23, where the error bars correspond to the standard deviation as measured from the observed scatter in the six sub-catalogs. From the figure it can be seen that the difference between the even and odd catalogs is negligible.

In Fig. 24 the galaxy counts derived from the EIS catalogs are compared to those of Lidman & Peterson (1996) and Postman et al. (1996). The  $1\sigma$  error bars are computed as above. There is a remarkable agreement between the EIS galaxy-counts and those of the other authors. The

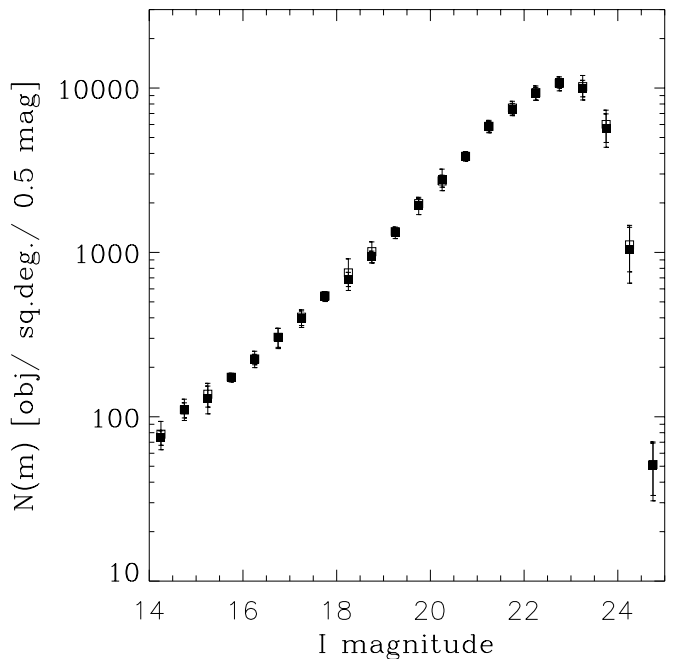


**Fig. 23.** The object counts as a function of magnitude as derived from the average of the counts in six odd (open squares) and even (filled squares) sub-catalogs. The error bars are the sample rms. In some cases the error bars are of the same size as the symbols

slope of the EIS counts is found to be  $0.43 \pm 0.01$ . Also note that the EIS counts extend beyond those of Postman et al. (1996) even for the counts derived from single frames. The galaxies have been defined to be objects with a stellarity index  $< 0.75$  for  $I < 21$  and all objects fainter than  $I = 21$ . At this limit galaxies already outnumber stars by a factor of  $\sim 3$ .

As discussed before, the criteria adopted for classifying stars and galaxies is somewhat arbitrary. While a large value for the stellarity index is desirable to extract a galaxy catalog as complete as possible, this may not be the most appropriate choice for extracting stellar samples. This can be seen in Fig. 25 where the EIS star-counts are shown for two different choices of the stellarity index for objects brighter than  $I = 21$ . For comparison, the star counts predicted by the galactic model of Méndez & van Altena (1996) are shown. As can be seen the observed counts agree with the model for low values of the stellarity index (0.5), while higher values shows a deficiency of stars at the faint-end.

These preliminary results based on single-frame catalogs indicate that the depth of the survey is close to that originally expected and is sufficiently deep, especially after coaddition, to search for distant clusters of galaxies, one of the main science goals of EIS.

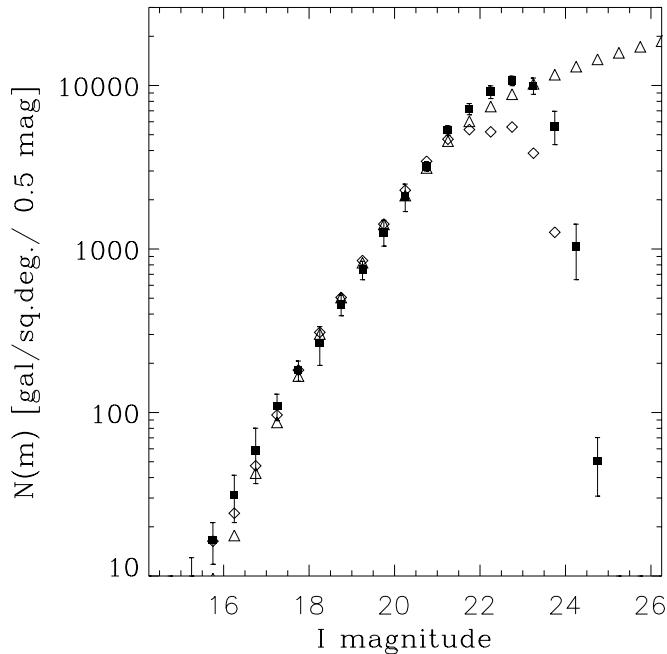


**Fig. 24.** The EIS galaxy counts (filled squares) with  $1\sigma$  error bars compared to the galaxy counts derived by Lidman & Peterson (1996) (triangles) and Postman et al. (1996) (diamond). The data from the other authors have been converted to the Johnson-Cousins system

**Table 4.** Number of Galaxies in Patch A

$m_{\text{lim}}$	Even		Odd	
	$N_{\text{gal}}$	$\bar{n}$ deg $^{-2}$	$N_{\text{gal}}$	$\bar{n}$ deg $^{-2}$
$m \leq 19$	2514	1056.3	2561	1076.0
$m \leq 20$	6972	2929.4	7072	2971.4
$m \leq 21$	18821	7908.0	19009	7987.0
$m \leq 22$	48129	20222.3	48316	20300.8
$m \leq 23$	94689	39785.3	95240	40016.8

## 6.2. Angular correlation function

In this section, the characteristics of the EIS catalogs are examined by computing the angular correlation function over the whole patch, for limiting magnitudes in the range  $I = 19$  to  $I = 23$ . Table 4 gives the number of galaxies down to the different magnitude limits. For comparison the odd and even catalogs are treated separately. The region defined by  $\alpha \gtrsim 340^\circ$  and  $\delta \gtrsim -39.8^\circ$  has been excluded from the analysis because of its known incompleteness (Sect. 6.3). Therefore, the total area used here is 2.38 square degrees.

To compute the angular correlation function, a random catalog is created with the same geometry as the EIS catalog. The number of random points has been chosen in order to yield an error less than 10% on the measured amplitude of  $w(\theta)$  at  $\theta = 5$  arcsec. The estimator used is that described by Landy & Szalay (1993):

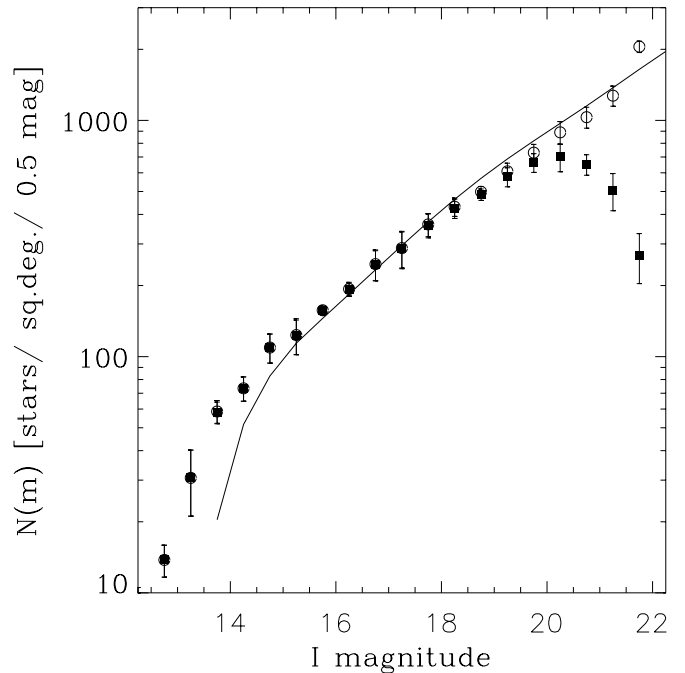


**Fig. 25.** The EIS star counts for stellerity index  $\geq 0.75$  (filled squares) and for stellerity index  $\geq 0.5$  (open circles) compared to the model by Mèndez & van Altena (1996) (solid line)

$$w(\theta) = \frac{DD - 2DR + RR}{RR}, \quad (1)$$

where  $DD$ ,  $DR$ , and  $RR$  are the number of data-data, data-random, and random-random pairs at a given angular separation  $\theta$ .

In Fig. 26,  $w(\theta)$  for the even and odd catalogs are compared. The error bars are  $1\sigma$  errors calculated with 10 bootstrap realizations. The angular correlation function  $w(\theta)$  is well described by a power-law  $\theta^{-\gamma}$  with  $\gamma \sim 0.8$  (shown by the dotted line) over the entire range of angular scales, extending out to  $\theta \sim 0.5$  degrees. In particular, there is no evidence for any feature related to the scale of the EMMI frame. Similar results are obtained when the angular correlation function is computed from counts-in-cells.

In Fig. 27, the amplitude,  $A_w(I)$ , of the correlation function at a scale of 1 arcsec is shown as a function of the limiting magnitude. The amplitude was computed from the best linear-fits over the range  $\sim 10 - 200$  arcsec of the  $w(\theta)$ , shown in Fig. 26, imposing a constant slope of  $\gamma = 0.8$ . For comparison, the power-law  $A_w \propto 10^{-0.27R}$ , originally determined by Brainerd et al. (1996) in the  $R$ -band is also shown corrected for the mean color difference  $(R - I) = 0.6$  (Fukugita et al. 1995). The agreement with previous results is excellent and demonstrates the good quality of the EIS catalogs, even for a patch observed under less than ideal conditions.

In order to evaluate the contribution of large-scale clustering to the variance in the galaxy counts computed in the previous section, the correlation function has been

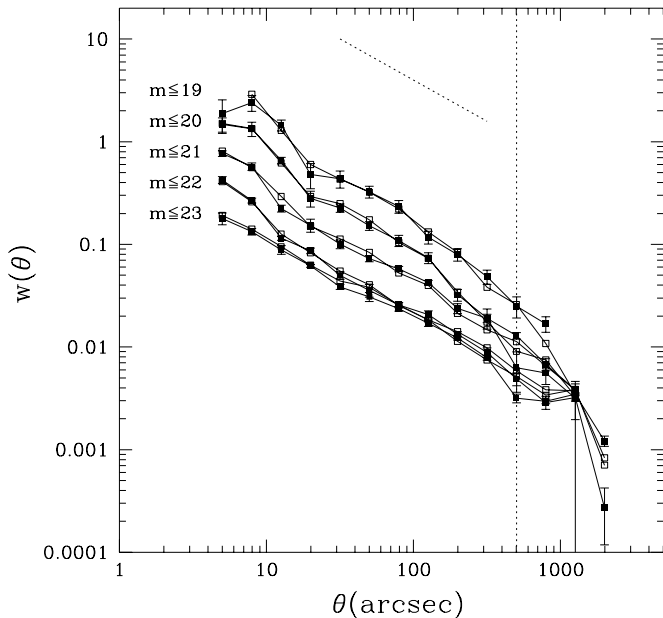


**Fig. 26.** Angular two-point correlation function calculated for the whole patch (even and odd catalogs) except the region defined by  $\alpha \gtrsim 340^\circ$  and  $\delta \gtrsim -39.8^\circ$  which has been removed for completeness problems. The dotted line represents a power-law with a slope of  $-0.8$

computed for the sub-areas also used in estimating the number counts. This offers the opportunity to compare the amplitude of the cosmic variance to the bootstrap errors used above. The results are shown in Fig. 28 where the mean value over the sub-areas of  $w(\theta)$  for each magnitude limit is presented. The error bars, that correspond to the rms of the six sub-areas, are consistent with those found from the bootstrap technique.

### 6.3. Field-to-field variations

The data for patch A are far from homogeneous and for some applications it is important to be able to objectively characterize the area and location of regions not suitable for analysis. A crude selection of these regions can be done by examining the distribution of the galaxy counts per frame as a function of the limiting magnitude. This is shown in Fig. 29 for the even and odd frames. The vertical lines correspond to the  $3\sigma$  deviations from the mean, where  $\sigma$  includes the contribution from Poisson fluctuations and the galaxy clustering. The latter was computed from counts-in-cells of galaxies on the scale of an EMMI-frame in the best available region of patch A.

The results show that for galaxies brighter than  $I = 20$ , all frames fall within the  $3\sigma$  level, except four, and the varying observing conditions do not seem to affect the completeness of these bright object catalogs. Going to fainter magnitudes the fraction of frames with low number counts increases. This can be used to estimate the size

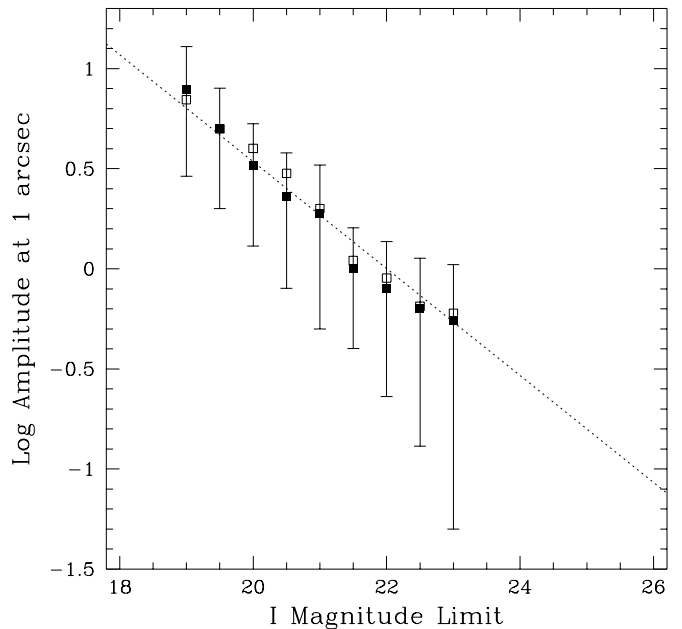


**Fig. 27.** Amplitude of the correlation function at 1 arcsec calculated from the best fits of Fig. 26 as a function of limiting magnitude. The dotted line is from Brainerd et al. (1996)

of the homogeneous part of the patch at a given limiting magnitude as shown in Fig. 30. From the figure, it can be seen that for  $I \sim 22$  and  $I \sim 23$  the useful area for analysis corresponds to  $\sim 90\%$  and  $\sim 75\%$ , respectively. Most of the rejected tiles are located in the region  $\alpha \gtrsim 340^\circ$  and  $\delta \gtrsim -40^\circ$  (Sect. 6.2).

## 7. Future prospects

The full release of the EIS-wide data, except for the  $U$ -band observations of patch B, is scheduled for July 1998. At that time, in addition to the calibrated frames and single-frame catalogs the coadded images and associated weight and context maps and catalogs will become available. Information relative to the contexts, which for coadded images replace the concept of a frame and is critical for the suitable characterization of the data for analysis purposes as was done in this paper on a frame basis. Only with the context maps it will be possible to extract sub-catalogs covering areas which fulfill particular requirements of homogeneity.

In parallel, the EIS pipeline will be revised and upgraded to handle data from CCD mosaics (SUSI2 and WFI@2.2), a key element for EIS-deep and the Pilot Survey envisioned for the first three months of operation of the ESO/MPIA 2.2 m telescope. One of the goals of the latter is to complete EIS-wide by providing multi-color coverage of some of the EIS patches already observed in the  $I$ -band. Another important task is to improve the data rate of the pipeline which will be essential to cope with the expected data flow from the 2.2 m telescope.

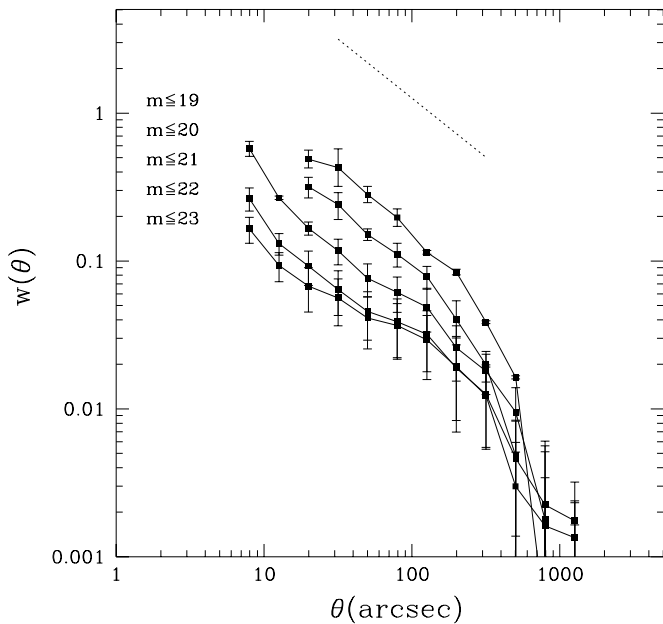


**Fig. 28.** Mean value of the angular correlation function measured for 6 sub-catalogs covering the whole patch. The error bars are the standard deviations calculated between these subsamples, and are therefore an estimate of the cosmic variance on the corresponding scales. The dotted line represents a power-law with a slope of  $-0.8$

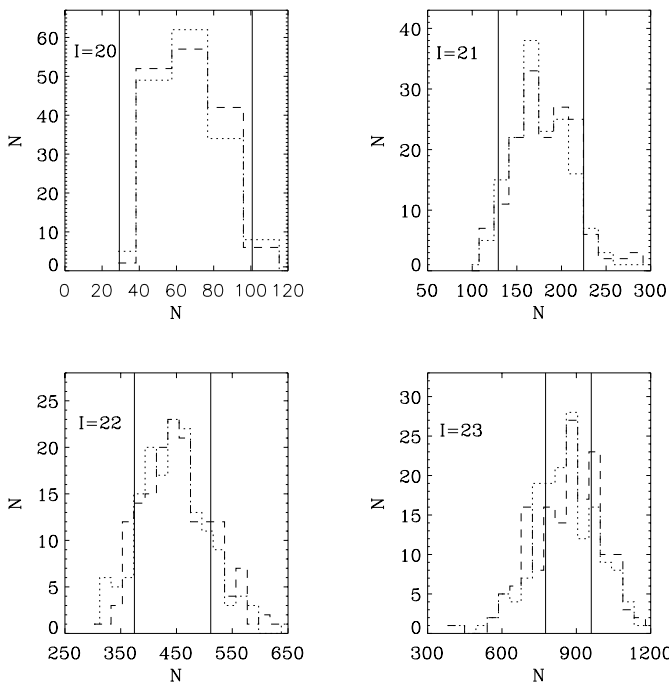


**Fig. 29.** Distribution of galaxy counts for the even (dotted line) and the odd (dashed line) catalogs as a function of limiting magnitude. The vertical lines correspond to the  $3\sigma$  deviations from the mean, where  $\sigma$  includes the contribution from Poisson fluctuations and the galaxy clustering

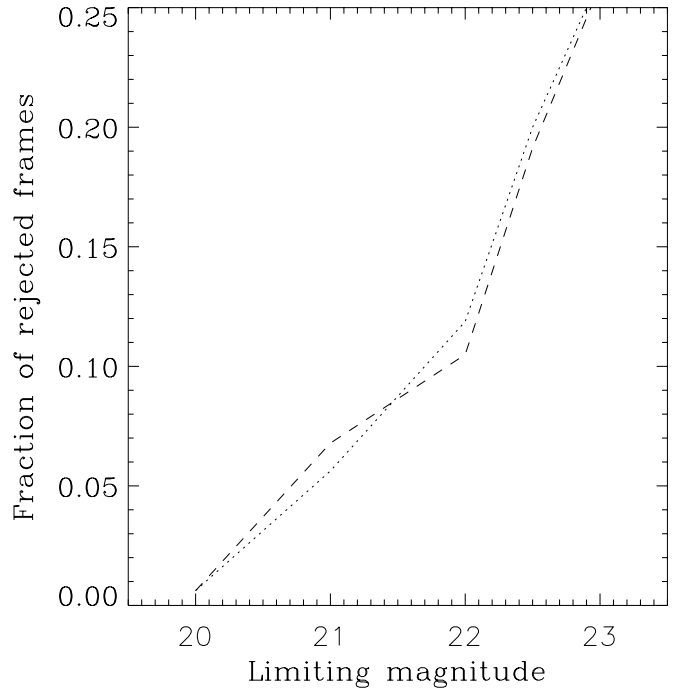


**Fig. 30.** Fraction of rejected tiles, corresponding to counts lower than  $3\sigma$  from the mean in Fig. 29, as a function of the limiting magnitudes

Complementing the EIS pipeline, software has also been implemented to produce derived catalogs which will also be made public. Priority has been given to searches of clusters of galaxies and preliminary results based on the single frames of patch A will be reported in separate papers of this series (Olsen et al. 1999).

All software and associated documentation will also be made available together with an in-depth discussion of the algorithms used in the pipeline (Deul et al. 1999). For the time being the upgraded SExtractor can be found in the EIS home page.

## 8. Summary

The ESO Imaging Survey is being carried out to help the selection of targets for the first year of operation of VLT. This paper describes the motivation, field and filter selection, and data reduction pipeline. Data for the first completed patch, in the form of astrometric and photometric calibrated pixel maps, single-frame catalogs, on-line coadded section images and further information on the project are available on the World Wide Web at “<http://www.eso.org/eis>”.

Preliminary evaluation of the data shows that the overall quality of the data is good and the completeness limit of the extracted catalogs is sufficiently deep to meet the science requirements of EIS. Furthermore, the results for the other patches should improve as the observing

conditions were considerably better than those in the period of patch A observations.

The final and complete release of the data products of EIS is scheduled as follows: 1) EIS-wide, except the *U*-band: July 31, 1998, before the first call for proposals for the VLT; 2) EIS-deep and EIS-wide *U*-band on December 31, 1998.

*Acknowledgements.* These data were taken at the New Technology Telescope (NTT) at the ESO La Silla Observatory under the ESO program identifications 59.A-9005(A) and 60.A-9005(A). We thank all the people directly or indirectly involved in the ESO Imaging Survey effort. In particular, all the members of the EIS Working Group for the innumerable suggestions and constructive criticisms, the ESO Archive Group, in particular M. Albrecht, for their support and for making available the computer facilities, ST-ECF for allowing some members of its staff to contribute to this enterprise. We also thank the Directors of all observatories and institutes listed in this paper as affiliations for allowing the participation of some of their staff in this project and for suggesting some of their students and post-docs to apply to the EIS visitor program. Special thanks to G. Miley, who facilitated the participation of ED in the project and for helping us secure observations from the Dutch 0.9 m telescope. To the Geneva Observatory, in particular G. Burki, for monitoring the extinction during most of the EIS observations. To the NTT team for their help. We are also grateful to N. Kaiser for the software and to the DENIS consortium for making available some of their survey data. The DENIS project development was made possible thanks to the contributions of a number of researchers, engineers and technicians in various institutes. The DENIS project is supported by the SCIENCE and Human Capital and Mobility plans of the European Commission under the grants CT920791 and CT940627, by the French Institut National des Sciences de l'Univers, the Education Ministry and the Centre National de la Recherche Scientifique, in Germany by the State of Baden-Württemberg, in Spain by the DGICYT, in Italy by the Consiglio Nazionale delle Ricerche, by the Austrian Fonds zur Förderung der wissenschaftlichen Forschung und Bundesministerium für Wissenschaft und Forschung, in Brazil by the Foundation for the development of Scientific Research of the State of São Paulo (FAPESP), and by the Hungarian OTKA grants F-4239 and F-013990 and the ESO C & EE grant A-04-046. Special thanks to A. Baker, D. Clements, S. Coté, E. Huizinga and J. Rönnback, former ESO fellows and visitors for their contribution in the early phases of the EIS project. Our special thanks to the efforts of A. Renzini, VLT Programme Scientist, for his scientific input, support and dedication in making this project a success. Finally, we would like to thank ESO's Director General Riccardo Giacconi for making this effort possible.

## References

- Baldwin J.A., Stone R.P.S., 1984, MNRAS 206, 241  
 Bertin E., 1999 (in preparation)  
 Bertin E., Arnouts S., 1996, A&AS 117, 393  
 Brighton A., 1998, VLT-MAN-ESO-19400-1552, Issue 1.0, Version 2.0.4, "The ESO SkyCat Tool Astronomical Image and Catalog Browser Programmer's Manual"  
 Brainerd T.G., Smail I.R., Mould J.R., 1995, MNRAS 275, 781  
 da Costa, et al., 1998a, The Messenger 91, 49  
 Deul E., et al., 1999 (in preparation)  
 Devillard N., 1997, <http://www.eso.org/eclipse>  
 D'Odorico S., 1990, The Messenger 61, 51  
 Epchtein N., et al., 1996, The Messenger 87, 27  
 Epchtein N., 1997, Proceedings of the Euroconference on "Impact of Large Scale Near-Infrared Surveys", Garzan F., Epchtein N., Omont A., Burton W.B., Persi P. (eds.). Kluwer Academic Publishers: Dordrecht  
 Erben T., 1996 (private communication)  
 Fruchter A.S., Hook R.N., 1997, in Applications of Digital Image Processing XX, Tescher A. (ed.), Proc. SPIE 3164, 120  
 Fukugita M., Shimasaku K., Ichikawa T., 1995, PASP 107, 945  
 Greisen E.W., Calabretta M., 1996, <http://www.cv.nrao.edu/fits/documents/wcs/wcs.html>  
 Gunn J.E., Stryker L.L., 1983, ApJS 52, 121  
 Hook R.N., Fruchter A.S., 1997, in ASP Conf. Ser. 125, Astronomical Data Analysis Software and Systems VI, Hunt G. and Payne H.E. (eds.). San Francisco: ASP, p. 147  
 Irwin M.J., 1985, MNRAS 214, 575  
 Kaiser N., Squires G., Broadhurst T., 1995, ApJ 449, 460  
 Kron R.G., 1980, ApJS 43, 305  
 Landolt A.U., 1992a, AJ 104, 340  
 Landolt A.U., 1992b, AJ 104, 372  
 Landy S.D., Szalay A.S., 1993, ApJ 412, 64  
 Lidman C., Peterson B., 1996, MNRAS 279, 1357  
 Mèndez R., van Altena W., 1996, AJ 112, 655  
 Olsen L.F., Scodreggio M., da Costa L.N., et al., 1999, A&A (submitted)  
 Postman M., Lubin L.M., Gunn J.E., et al., 1996, AJ 111, 615  
 Renzini A., da Costa L.N., 1997, The Messenger 87, 23  
 Renzini A., 1998, The Messenger 91, 54  
 Villumsen, et al., 1998 (private communication)  
 White R., 1992, <http://www.stsci.edu/software/hcompress.html>